ATLAS CONF Note

CONF-EXOT-2020-048

31st July 2020

Search for new phenomena in events with jets and missing transverse momentum in pp collisions at $\sqrt{s} = 13$ TeV with the ATLAS detector

The ATLAS Collaboration

Results of a search for new physics in final states with an energetic jet and large missing transverse momentum are reported. The search uses proton–proton collision data corresponding to an integrated luminosity of 139 fb^{-1} at a centre-of-mass energy of 13 TeV collected in the period 2015–2018 with the ATLAS detector at the Large Hadron Collider. Compared to previous publications, in addition to an increase of almost a factor of four in the data size, the analysis implements a number of improvements in the signal selection and the background determination leading to enhanced sensitivity. Events are required to have at least one jet with transverse momentum above 150 GeV and no reconstructed leptons (e, μ or τ) or photons. Several signal regions are considered with increasing requirements on the missing transverse momentum starting at 200 GeV. An overall agreement is observed between the number of events in data and Standard Model predictions. Model-independent 95% confidence level limits on visible cross sections for new processes are obtained in the range between 861 fb and 0.3 fb. Results are also translated into improved exclusion limits in models with pair-produced weakly interacting dark-matter candidates, large extra spatial dimensions, supersymmetric particles in several compressed scenarios, axion-like particles, and new scalar particles in dark-energy inspired models. In addition, the data are translated into bounds on the invisible branching ratio of the Higgs boson.

ATLAS-CONF-2020-048
14 August 2020

1 Introduction

This paper presents the results of a new search for new phenomena in events containing an energetic jet and large missing transverse momentum $\mathbf{p}_{\mathrm{T}}^{\mathrm{miss}}$ (with magnitude $E_{\mathrm{T}}^{\mathrm{miss}}$) in proton–proton collisions at a centre-of-mass energy $\sqrt{s} = 13$ TeV collected by the ATLAS Collaboration at the Large Hadron Collider (LHC). The final-state monojet signature of at least one energetic jet, $E_{\mathrm{T}}^{\mathrm{miss}} > 200$ GeV, and no leptons constitutes a distinctive signature for new physics beyond the Standard Model (SM) at colliders.

In this publication, a data sample corresponding to a total integrated luminosity of 139 fb^{-1} is used, and the analysis strategy follows closely that of the previous publication based on 36.1 fb^{-1} [1]. In addition, a number of improvements are implemented leading to enhanced sensitivity to new phenomena. The p_{T} requirements for identifying electrons and muons in the final state are lowered, translating into tighter lepton vetoes and a larger background reduction, which is also complemented with the inclusion of τ-lepton and photon vetoes. The kinematic range covered by the analysis is extended towards lower thresholds on $E_{\mathrm{T}}^{\mathrm{miss}}$ and leading-jet p_{T}, and new control regions are defined for a better determination of backgrounds related to top-quark and Z-boson production processes. Finally, the analysis profits from improved theoretical predictions for W+jets and Z+jets production, including higher order corrections at next-to-next-to-leading-order (NNLO) in QCD and next-to-leading-order (NLO) in electroweak couplings supplemented by Sudakov logarithms at two loops.

The monojet signature has been extensively studied at the LHC in the context of searches for large extra spatial dimensions (LED), supersymmetry (SUSY), weakly interacting massive particles (WIMPs) as candidates for dark matter (DM) [1–5], and dark energy (DE) inspired models leading to the production of new scalar particles in the final state [6]. In addition, experimental results have been re-interpreted in terms of new theoretical scenarios with axion-like particles [7]. Finally, the monojet final state results have been used to constrain the invisible branching fraction of the Higgs boson [8, 9]. In the following, the different models are briefly discussed. Figure 1 shows diagrams for some of the models.

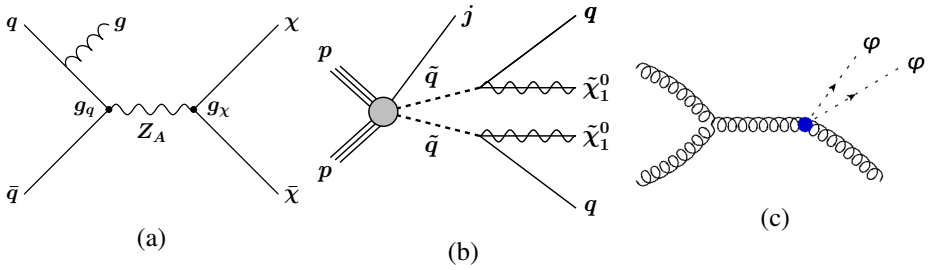

Figure 1: (a) Diagram for the pair-production of weakly interacting massive particles χ, with a mediator Z_A with axial-vector couplings exchanged in the s-channel. (b) A generic diagram for the pair-production of squarks with the decay mode $\tilde{q} \to q + \tilde{\chi}_1^0$. The presence of a jet from initial-state radiationis indicated for illustration purposes. (c) Diagram for the pair production of dark energy scalar fields φ in association with an energetic jet in the final state.

The existence of a non-baryonic form of matter is well established from a number of astronomical observations [10–12]. The existence of a new, weakly interacting massive particle is often hypothesized [13], as it leads to the correct relic density for non-relativistic matter in the early universe [14] as measured from data from the Planck [15] and WMAP [16] Collaborations. For WIMP masses below one TeV, WIMPs may be pair-produced at the LHC. Traditionally, the monojet-like final state has been considered a golden channel for the discovery of WIMPs at colliders. In this case, the WIMP pair is produced in association

with a jet of particles from initial-state radiation, leading to the signature of a jet and missing transverse momentum (see Fig. 1(a)). Results are presented for simplified DM models [17–19] where Dirac fermion WIMPs (χ) are pair-produced from quarks via s-channel exchange of a spin-1 mediator particle (Z_A) or a spin-0 mediator particle (Z_P) with axial-vector or pseudoscalar couplings, respectively. In the case of the axial-vector mediator model, mediator masses below 1.55 TeV have been already excluded at 95% CL for very light WIMPs in previous analyses [1].

Supersymmetry is a theory of physics beyond the SM which can solve naturally the hierarchy problem and can provide candidates for dark matter [20–28]. SUSY introduces a new supersymmetric partner (sparticle) for each particle in the SM. Specifically, a new scalar field is associated with each quark chirality state. Two squark mass eigenstates $\tilde{q}_1$ and $\tilde{q}_2$ result from the mixing of the scalar fields for a particular flavour. In supersymmetric extensions of the SM that assume R-parity conservation [29–33], sparticles are produced in pairs and the lightest supersymmetric particle (LSP) is stable. The LSP is assumed to be the lightest neutralino $\tilde{\chi}_1^0$. The results are interpreted in terms of searches for squark production using simplified models in scenarios for which the mass difference $\Delta m \equiv m_{\tilde{q}} - m_{\tilde{\chi}_1^0}$ is small (compressed-mass scenario). In this case, the p_{T} of the resulting quark jets and the $E_{\mathrm{T}}^{\mathrm{miss}}$ in the final state are both small, making it difficult to reconstruct the SUSY signal. The monojet signature provides unique access to this parameter space, for which the presence of jets from initial-state radiation (ISR) is used to identify signal events, leading to larger $E_{\mathrm{T}}^{\mathrm{miss}}$ (see Fig. 1(b)). In the case of bottom-squark (sbottom) and top-squark (stop) pair production in a compressed-mass supersymmetric scenario, squark masses below about 430 GeV have been already excluded at 95% CL [1].

The origin of the accelerating expansion of the universe [34, 35] is, together with the nature of the dark matter, a major open question in cosmology. The theoretical understanding of the accelerating expansion of the Universe in terms of fundamental physics, beyond the ad hoc adoption of a cosmological constant in general relativity, often involves the introduction of additional scalars interacting with both gravity and matter fields [36]. Here an effective field theory implementation of the Horndeski theories [37] is considered [38] introducing a new dark energy scalar field φ, governed by an effective mass M_2 and a coupling g^* to matter, which is considered universal. For the model relevant for this case, the new scalar particle is stable and is produced in pairs leaving the experiment undetected. When they are produced in association with an energetic gluon, it leads to a monojet final state topology (see Fig. 1(c)). Previous results [6] indicate no sensitivity for $g* \leq 1.8$ and values for M_2 below 1.2 TeV have been excluded at 95% CL for $g^* \geq 3.5$.

Large extra spatial dimensions have been postulated to explain the large difference between the electroweak unification scale at $O(10^2)$ GeV and the Planck scale M_{Pl} at $O(10^{19})$ GeV. In the Arkani-Hamed, Dimopoulos, and Dvali (ADD) model of LED [39], the presence of n extra spatial dimensions of size R leads to a fundamental Planck scale in $4 + n$ dimensions given by ${M_{\mathrm{Pl}}}^2 \sim {M_D}^{2+n} R^n$, where M_D is the fundamental scale of the $4 + n$-dimensional theory. The extra spatial dimensions are compactified, resulting in a Kaluza–Klein tower of massive graviton modes (KK graviton). If produced in high-energy proton–proton collisions in association with a jet of hadrons, a KK graviton escaping into the extra dimensions can be inferred from $E_{\mathrm{T}}^{\mathrm{miss}}$, and can lead to a monojet event signature. Values of M_D below 7.7 TeV at $n = 2$ and below 4.8 TeV at $n = 6$ have been already excluded at 95% CL [1].

New pseudo-scalar bosons, denoted as axion-like particles (ALPs), are introduced in different models involving the breaking of additional U(1) symmetries. The existence of axions was postulated [40] to address the strong CP problem for which an anomalous global U(1) symmetry is spontaneously broken. Axions are candidates for explaining the dark matter content of the universe. The strength of the coupling

between the axions and the ordinary matter is governed by the electroweak symmetry breaking scale, leading to rather strong constraints. Other models with ALPs, going beyond the minimal QCD axion realization, consider much weaker interactions suppressed by a much higher scale [7, 41]. In this paper, an effective implementation of an ALP model (with an effective scale f_a) is considered, in which ALPs are produced in association with a gluon in a final state governed by an ALP-gluon coupling $c_{\tilde{G}}$. By construction, ALP decays are suppressed and the ALP leaves the detector undetected, leading to a monojet final state topology.

A variety of models of WIMP dark matter at the LHC involve the Higgs boson acting as a portal between the dark sector and the SM sector, either via direct Yukawa couplings to fermionic dark matter candidates or via other mechanisms. The decay of the Higgs boson into dark matter particles translates into a signature of $E_{\mathrm{T}}^{\mathrm{miss}}$ in the final state. Searches for invisible Higgs boson decays have been carried out at ATLAS and CMS, considering different SM Higgs production processes and different centre-of-mass energies, leading to a 95% confidence level (CL) upper limit on the invisible Higgs boson branching ratio of 0.26 [42] and 0.19 [43], respectively.

The paper is organized as follows. The ATLAS detector is described in the next Section. Section 3 provides details of the Monte Carlo simulations used in the analysis for background and signal processes. Section 4 discusses the reconstruction and identification of jets, leptons, and missing transverse momentum, while Section 5 describes the event selection. The estimation of background contributions and the study of systematic uncertainties are discussed in Sections 6 and 7. The results are presented in Section 8 and are interpreted in terms of limits in models of WIMP-pair production, ADD, SUSY in compressed scenarios, axion-like particles, new bosons in DE inspired models, and limits on the Higgs boson invisible branching fraction. Finally, Section 9 is devoted to the conclusions.

2 ATLAS detector

The ATLAS detector [44] at the LHC covers nearly the entire solid angle around the collision point.[1] It consists of an inner tracking detector surrounded by a thin superconducting solenoid, electromagnetic and hadronic calorimeters, and a muon spectrometer incorporating three large superconducting toroidal magnets. The inner-detector system (ID) is immersed in a 2 T axial magnetic field and provides charged-particle tracking in the range $|\eta| < 2.5$.

The high-granularity silicon pixel detector covers the vertex region and typically provides four measurements per track, the first hit being normally in the insertable B-layer (IBL) installed before Run 2 [45, 46]. It is followed by the silicon microstrip tracker (SCT) which usually provides eight measurements per track. These silicon detectors are complemented by the transition radiation tracker (TRT), which enables radially extended track reconstruction up to $|\eta| = 2.0$. The TRT also provides electron identification information based on the fraction of hits (typically 30 in total) above a higher energy-deposit threshold corresponding to transition radiation.

The calorimeter system covers the pseudorapidity range $|\eta| < 4.9$. Within the region $|\eta| < 3.2$, electromagnetic calorimetry is provided by barrel and endcap high-granularity lead/liquid-argon (LAr)

[1] ATLAS uses a right-handed coordinate system with its origin at the nominal interaction point (IP) in the centre of the detector and the z-axis along the beam pipe. The x-axis points from the IP to the centre of the LHC ring, and the y-axis points upwards. Cylindrical coordinates (r, ϕ) are used in the transverse plane, ϕ being the azimuthal angle around the z-axis. The pseudorapidity is defined in terms of the polar angle θ as $\eta = -\ln\tan(\theta/2)$. Angular distance is measured in units of $\Delta R \equiv \sqrt{(\Delta\eta)^2 + (\Delta\phi)^2}$.

calorimeters, with an additional thin LAr presampler covering $|\eta| < 1.8$, to correct for energy loss in material upstream of the calorimeters. Hadronic calorimetry is provided by the steel/scintillating-tile calorimeter, segmented into three barrel structures within $|\eta| < 1.7$, and two copper/LAr hadronic endcap calorimeters. The solid angle coverage is completed with forward copper/LAr and tungsten/LAr calorimeter modules optimised for electromagnetic and hadronic measurements respectively.

The muon spectrometer (MS) comprises separate trigger and high-precision tracking chambers measuring the deflection of muons in a magnetic field generated by superconducting air-core toroids. The field integral of the toroids ranges between 2.0 and 6.0 T m across most of the detector. A set of precision chambers covers the region $|\eta| < 2.7$ with three layers of monitored drift tubes, complemented by cathode-strip chambers in the forward region, where the background is highest. The muon trigger system covers the range $|\eta| < 2.4$ with resistive-plate chambers in the barrel, and thin-gap chambers in the endcap regions.

Events of interest are selected to be recorded by the first-level trigger system implemented in custom hardware, followed by selections made by algorithms implemented in software in the high-level trigger [47]. The first-level trigger reduces the 40 MHz bunch crossing rate to below 100 kHz, which the high-level trigger further reduces in order to record events to disk at about 1 kHz.

3 Monte Carlo simulation

Monte Carlo (MC) simulated event samples are used to compute detector acceptance and reconstruction efficiencies, determine signal and background contributions, and estimate systematic uncertainties in the final results. The SM background samples are processed with the full ATLAS detector simulation [48] based on GEANT4 [49]. Signal simulated samples, with the exception of those for Higgs production, are processed with a fast simulation using a parameterisation of the calorimeter response and Geant4 for the other parts of the detector. The EvtGen v1.2.0 program [50] is used to model the decays of the bottom and charm hadrons. Simulated events are then reconstructed and analysed with the same analysis chain as for the data, using the same trigger and event selection criteria. The effects of multiple proton–proton interactions in the same or neighbouring bunch-crossings (pile-up) are taken into account by overlaying simulated minimum-bias events from PYTHIA 8.186 [51] with the A3 set of tuned parameters (tune) [52] and the NNPDF2.3LO PDF set [53] onto the hard-scattering process, distributed according to the frequency in data. Correction factors are applied to the Monte Carlo simulation to account for differences between simulation and the data in pile-up, energy and momentum scales and reconstruction and identification efficiencies of physics objects.

3.1 Signal simulation

Simulated samples for the ADD LED model with different numbers of extra dimensions in the range $n = 2$–6 and a fundamental scale M_D in the range 3–12 TeV are generated using PYTHIA 8.205 with the A14 tune [54] and NNPDF2.3LO parton distribution functions (PDFs). The renormalization scale is set to the geometric mean of the squared transverse masses of the two produced particles, $\sqrt{(p_{\mathrm{T},G}^2 + m_G^2)(p_{\mathrm{T},p}^2 + m_p^2)}$, where $p_{\mathrm{T},G}$ and m_G ($p_{\mathrm{T},p}$ and m_p) denote, respectively, the transverse momentum and the mass of the KK graviton (parton) in the final state. The factorization scale is set to the minimum transverse mass, $\sqrt{p_{\mathrm{T}}^2 + m^2}$, of the KK graviton and the parton.

SUSY signals for squark-pair production are generated with MadGraph5_aMC@NLO v2.2.3 [55] and interfaced to Pythia 8.186 with the A14 tune for modelling of the squark decay, parton showering, hadronization, and the underlying event. The PDF set used for the generation is NNPDF23LO, and the renormalization and factorization scales are set to $\mu = \sum_i \sqrt{m_i^2 + p_{T,i}^2}$, where the sum runs over all final-state particles from the hard-scatter process. The matrix-element calculation is performed at tree level, and includes the emission of up to two additional partons. Matching to parton-shower calculations is accomplished by the CKKW-L prescription [56], with a matching scale set to one quarter of the pair-produced superpartner mass. All signal cross sections are calculated to approximate next-to-next-to-leading order (NNLO) in the strong coupling constant, adding the resummation of soft gluon emission at next-to-next-to-leading-logarithm accuracy (approximate NNLO+NNLL) [57–60] The nominal cross section and its uncertainty are taken from an envelope of cross-section predictions using different PDF sets and factorization and renormalization scales, as discussed in Ref. [61]. Simulated samples are produced with squark masses in the range between 250 GeV and 1.2 TeV, and squark–neutralino mass differences Δm varying between 5 GeV and 50 GeV.

WIMP s-channel signal samples are simulated in Powheg-Box v2 [62–64] (revision 3049) using two implementations of simplified models, introduced in Ref. [65]. The DMV model of WIMP-pair production is used for s-channel spin-1 axial-vector mediator exchange at NLO in the strong coupling constant, and the DMS_tloop model is used for WIMP-pair production with the s-channel spin-0 pseudoscalar mediator exchange with the full quark-loop calculation at leading order (LO) [66]. Renormalization and factorization scales are set to $H_{\mathrm{T}}/2$ on an event-by-event basis, where $H_{\mathrm{T}} = \sqrt{m_{\chi\chi}^2 + p_{\mathrm{T},j1}^2} + p_{\mathrm{T},j1}$ is defined by the invariant mass of the WIMP pair ($m_{\chi\chi}$) and the transverse momentum of the highest-p_{T} parton-level jet ($p_{\mathrm{T},j1}$). The mediator propagator is described by a Breit–Wigner distribution. Events are generated using the NNPDF30 [53] PDFs and interfaced to Pythia 8.205 with the A14 tune [67] for parton showering, hadronization and the underlying event. Couplings of the mediator to WIMP particles and those of the SM quarks are set to $g_\chi = 1$ and $g_q = 1/4$, respectively, for the axial-vector mediator model whereas both couplings are set to one in the case of the pseudoscalar mediator model, following the conventions of the LHC DM WG [17, 18]. Each model is simulated for a range of possible WIMP and mediator masses, with WIMP masses ranging from 1 GeV to 1 TeV and mediator masses between 10 GeV and 10 TeV.

Samples of simulated events for ALP production in association with a jet [41] are generated with MG5_aMC@NLO v2.6.2 and interfaced to Pythia 8.240 with the A14 tune for modelling of parton showering, hadronization, and the underlying event. The PDF set used for the generation is NNPDF23LO, and the renormalization and factorization scales are set to half of transverse mass, $0.5 \times \sqrt{p_{\mathrm{T}}^2 + m^2}$, of the ALP and the parton. Other processes related to the coupling of the ALP to photons, vector bosons or the Higgs boson are suppressed. The ALP mass and the coupling to gluons are initially set to $m_a = 1$ MeV and $c_{\tilde{G}} = 1$, respectively. Effective scales f_a in the range between 1 TeV and 10 TeV are explored.

Simulated events for the dark energy model have been generated using an effective field theory implementation [36] in MG5_aMC@NLO v2.6.1. Following the work in Ref. [6], only terms corresponding to the $\mathcal{L}_2$ operator, relevant for the monojet final state topology, are considered with Wilson coefficient $c_2 = 1$ and the rest of Wilson coefficients (c_i) set to zero. Electroweak terms are vetoed and only one insertion of a $\mathcal{L}_2$ operator in each diagram is allowed. The generated events are interfaced to Pythia 8.240 with the A14 tune for modelling of parton showering, hadronization, and the underlying event. The PDF set used for the generation is NNPDF23LO, and the renormalization and factorization scales are set to $0.5 \times H_{\mathrm{T}} = \sqrt{m_{\varphi\varphi}^2 + p_{\mathrm{T},j1}^2} + p_{\mathrm{T},j1}$, where $m_{\varphi\varphi}$ is the invariant mass of the two scalar particles in the

final state. The dark energy field mass and the coupling to gluons are set to $m_\varphi = 100$ MeV and $g^* = 4\pi$, respectively. Effective scales M_2 up to 3 TeV are explored.

Simulated samples for the production of a 125 GeV Higgs boson have been generated, with NLO accuracy in QCD emissions, using the POWHEG-BOX v2 [68] event generator. The samples include gluon-gluon initiated processes ($gg \to H$), vector boson fusion (VBF) driven processes ($VV \to H$), and the associated production with a W/Z boson in the final state (VH). The simulated events are interfaced with Pythia 8.212 for parton shower, hadronization and underlying event modelling using the AZNLO tune [69] with the NNPDF30+CTEQ6L1 PDF in the case of $gg \to H$, and CT10 and NNPDF30 PDF in the case of VH and $VV \to H$ processes, respectively. The $gg \to H$ sample is normalized such that it reproduces the total cross section predicted by a next-to-next-to-next-to-leading-order (NNNLO) QCD calculation with NLO electroweak corrections applied, and $VV \to H$ and VH processes are normalized to cross sections calculated at NNLO in QCD with NLO electroweak corrections [70]. The contribution from processes involving the Higgs boson in association with top-quarks in the final state is negligible. In all cases, the Higgs boson invisible decay $H \to Z^*Z \to 4\,\nu$ is considered, which provides final-state topologies consistent with those from models for new phenomena with invisibly decaying Higgs bosons.

3.2 Background simulation

After applying the final state selection as described in Section 5, the primary SM background contributing to monojet event signatures is $Z \to \nu\nu$ + jets. There are also significant contributions from W + jets events, primarily from $W \to \tau\nu$ + jets, with non-identified leptons in the final state. Small contributions are expected from $Z \to \ell\ell$ + jets ($\ell = e, \mu, \tau$), multijet, $t\bar{t}$, single-top, and diboson (WW, WZ, ZZ) processes. Contributions from top-quark production associated with additional vector bosons ($t\bar{t} + W$, $t\bar{t} + Z$, or $t + Z + q/b$ processes) are negligible and not considered in this analysis. As discussed in detail in Section 6, the contribution from SM background processes in the signal regions are determined using simulated samples constrained with data in control regions. In the following, the generation of the different simulation samples is described.

Events containing W or Z bosons with associated jets are simulated using the SHERPA 2.2.1 [71] event generator. Matrix elements (ME) are calculated for up to two partons at NLO and four partons at LO using OpenLoops [72] and Comix [73], and merged with the SHERPA parton shower (PS) [74] using the ME+PS@NLO prescription [75]. The NNPDF3.0NNLO [53] PDF set is used in conjunction with a dedicated parton-shower tuning developed by the authors of SHERPA. The MC predictions are initially normalized to NNLO perturbative QCD (pQCD) predictions according to DYNNLO [76, 77] using the MSTW2008 90% CL NNLO PDF set [78].

In order to improve the description of W+jets and Z+jets processes, their MC predictions are reweighted to account for higher-order QCD and electroweak corrections [79], where parton-level predictions for W/Z+jets production, including NNLO QCD corrections and NLO electroweak corrections supplemented by Sudakov logarithms at two loops, are provided as a function of the vector-boson p_{T}, improving the description of the measured Z-boson p_{T} distribution [80]. The predictions are provided separately for the different W+jets and Z+jets processes together with the means for a proper estimation of theoretical uncertainties and their correlations (see Section 7). The reweighting procedure takes into account the difference between the QCD NLO predictions as included already in SHERPA and as provided by the parton-level calculations.

Separate non-overlapping samples for W/Z+jets production via VBF driven processes are generated using HERWIG 7.1.5 [81]. The samples are produced at NLO accuracy in pQCD using VBFNLO v3.0.0 [82]. The NNPDF30 PDF set is used along with the default set of tuned parameters for parton showering, hadronization and underlying event.

For the generation of $t\bar{t}$ and single top-quarks events in the Wt-channel and s-channel, the Powheg-Box v2 [68] event generator is used with CT10 [83] PDFs. Electroweak t-channel single-top-quark events are generated using the Powheg-Box v1 event generator. This event generator uses the four-flavour scheme to calculate NLO matrix elements, with the CT10 four-flavour PDF set. Interference occurring beyond tree level between Wt and $t\bar{t}$ processes is studied considering both diagram subtraction (DS) and diagram removal (DR) production schemes [84]; DR is used for the nominal background prediction, DS for the evaluation of systematic uncertainties as described in Sec. 7. The samples are normalized to NNLO pQCD predictions. The parton shower, hadronization, and underlying event are simulated using Pythia 8.205 with the A14 tune. The top-quark mass is set to 172.5 GeV. Alternative samples are generated using MadGraph5_aMC@NLO (v2.2.1) and Powheg-Box interfaced to Herwig++ (v7.1.3) [81] in order to estimate the effects of the choice of matrix-element event generator parton-shower algorithm, fragmentation and hadronization effects.

Diboson samples (WW, WZ, and ZZ production) are generated using Sherpa 2.2.1 or Sherpa 2.2.2 with NNPDF3.0NNLO, and are normalized to NLO pQCD predictions [85].

4 Event reconstruction

Jets are reconstructed from energy deposits in the calorimeters using the anti-k_t jet algorithm [86] as provided by the fastjet [87] toolkit, with the radius parameter $R = 0.4$. The measured jet four-momentum is calibrated using information from both simulation and data [88]. In addition, jets are corrected for contributions from pile-up [89]. Jets with $p_{\mathrm{T}} > 20\,\mathrm{GeV}$ and $|\eta| < 2.8$ are considered in the analysis. A combination of track-based variables developed to suppress pile-up jets, called the jet-vertex tagger [90], is constructed. In order to remove jets originating from pile-up collisions, for central jets ($|\eta| < 2.4$) with $p_{\mathrm{T}} < 50\,\mathrm{GeV}$ a significant fraction of the tracks associated with each jet must have an origin compatible with the primary vertex, as defined by the jet-vertex tagger.

Jets with $p_{\mathrm{T}} > 30\,\mathrm{GeV}$ and $|\eta| < 2.5$ are identified as jets containing B-hadrons (b-jets) if tagged by a multivariate algorithm which uses information about the impact parameters of inner-detector tracks matched to the jet, the presence of displaced secondary vertices, and the reconstructed flight paths of b- and c-hadrons inside the jet [91, 92]. A 60% efficient b-tagging working point, as determined in a simulated sample of $t\bar{t}$ events, is chosen. This corresponds to rejection factors of approximately 1500, 35 and 180 for light-quark and gluon jets, c-jets, and τ-leptons decaying hadronically, respectively.

Electrons are found by combining energy deposits in the calorimeter with tracks found in the inner detector. They are initially required to have $p_{\mathrm{T}} > 7\,\mathrm{GeV}$ and $|\eta| < 2.47$, to satisfy the 'Loose' electron shower shape and track selection criteria described in [93], including a requirement on the match between the track and the primary vertex, based on the requirement on the longitudinal impact parameter $|z_0| \sin\theta$ to be less than 0.5 mm. Overlaps between identified electrons and jets with $p_{\mathrm{T}} > 30\,\mathrm{GeV}$ in the final state are resolved. Jets are discarded if they are not b-tagged and their separation $\Delta R = \sqrt{(\Delta\eta)^2 + (\Delta\phi)^2}$ from an identified electron is less than 0.2. Otherwise, the electron is removed as it most likely originates from a semileptonic b-hadron decay. The electrons separated by ΔR between 0.2 and 0.4 from any remaining jet are removed.

Muon candidates are formed by combining information from the muon spectrometer and inner tracking detectors. They are required to pass 'Medium' identification requirements [94], and to have $p_{\mathrm{T}} > 7\,\mathrm{GeV}$ and $|\eta| < 2.5$. As in the case of electrons, the muon track is required to have $|z_0| \sin\theta < 0.5\,\mathrm{mm}$. Jets with $p_{\mathrm{T}} > 30\,\mathrm{GeV}$ and fewer than three tracks with $p_{\mathrm{T}} > 500\,\mathrm{MeV}$ associated with them are discarded if their separation ΔR from an identified muon is less than 0.4. The muon is discarded if it is matched to a jet with $p_{\mathrm{T}} > 30\,\mathrm{GeV}$ that has at least three tracks associated with it. If an electron and a muon share the same inner detector track, the muon is retained and the electron is discarded, in order to remove electron candidates originating from muon bremsstrahlung followed by photon conversion.

Hadronically-decaying τ-lepton candidates are formed by combining information from the calorimeters and inner tracking detectors. The τ-lepton reconstruction algorithm [95] is seeded by jets reconstructed with $p_{\mathrm{T}} > 10\,\mathrm{GeV}$ and $|\eta| < 2.5$, and the reconstructed energies of the τ-lepton candidates are corrected to the τ-lepton energy scale [96]. They are required to pass 'Loose' identification requirements [97], to have $p_{\mathrm{T}} > 20\,\mathrm{GeV}$, $|\eta| < 2.5$ excluding the transition region between the EM barrel and endcap calorimeters ($1.37 < |\eta| < 1.52$), and to have 1 or 3 associated charged tracks. The τ-leptons close to electrons or muons ($\Delta R < 0.2$) are removed. Any jet within $\Delta R = 0.2$ of a τ-lepton is removed.

Photons are reconstructed from clusters of energy deposited in the EM calorimeter. They are required to pass 'Tight' identification requirements [98], to have $p_{\mathrm{T}} > 10\,\mathrm{GeV}$ and $|\eta| < 2.37$. Photons are discarded if their separation ΔR from an identified muon or electron is less than 0.4. Jets are instead discarded if their separation ΔR from an identified photon is less than 0.4.

The vector missing transverse momentum $\mathbf{p}_{\mathrm{T}}^{\mathrm{miss}}$ is reconstructed from the negative vectorial sum of the transverse momenta of electrons, muons, τ-leptons, photons, and jets with $p_{\mathrm{T}} > 20\,\mathrm{GeV}$ and $|\eta| < 4.5$. Tracks compatible with the primary vertex but not associated to any of those objects are also included in the vectorial sum, as described in Sec. 3.4.2 of Ref. [99].

5 Event selection

This analysis is based on data collected by ATLAS throughout Run-2 of the LHC, corresponding to a total integrated luminosity of $139\,\mathrm{fb}^{-1}$. The data were collected using a trigger based on a requirement on $E_{\mathrm{T}}^{\mathrm{miss}}$ as computed from calorimetry information at the final stage of the two-level trigger system [100]. After analysis selections, the trigger was measured to be fully efficient for events with $E_{\mathrm{T}}^{\mathrm{miss}} > 200\,\mathrm{GeV}$, as determined using a data sample with muons in the final state.

Events are required to have at least one reconstructed primary vertex consistent with the beamspot envelope and that contains at least two associated tracks of $p_{\mathrm{T}} > 500\,\mathrm{MeV}$. When more than one such vertex is found, the vertex with the largest summed p_{T}^2 of the associated tracks is chosen. Events having identified muons, electrons, photons or τ-leptons in the final state are vetoed. Events are selected with $E_{\mathrm{T}}^{\mathrm{miss}} > 200\,\mathrm{GeV}$, a leading jet with $p_{\mathrm{T}} > 150\,\mathrm{GeV}$ and $|\eta| < 2.4$, and a maximum of four jets with $p_{\mathrm{T}} > 30\,\mathrm{GeV}$ and $|\eta| < 2.8$. Separation in the azimuthal angle of $\Delta\phi(\mathrm{jet}, \mathbf{p}_{\mathrm{T}}^{\mathrm{miss}}) > 0.4(0.6)$ between the missing transverse momentum direction and each selected jet is required for events with $E_{\mathrm{T}}^{\mathrm{miss}} > 250\,\mathrm{GeV}$ ($200\,\mathrm{GeV} < E_{\mathrm{T}}^{\mathrm{miss}} \leq 250\,\mathrm{GeV}$) to reduce the multijet background contribution, where a large $E_{\mathrm{T}}^{\mathrm{miss}}$ can originate from jet energy mismeasurement. Jet quality criteria [101] are imposed, which involve selections based on quantities such as the pulse shape of the energy depositions in the cells of the calorimeters, electromagnetic fraction in the calorimeter, maximum fraction of the jet energy collected by a single

Table 1: Intervals and labels of the $E_{\mathrm{T}}^{\mathrm{miss}}$ bins used for the signal region. See the text for details.

Exclusive (EM)	EM0	EM1	EM2	EM3	EM4	EM5	EM6
$E_{\mathrm{T}}^{\mathrm{miss}}$ [GeV]	200–250	250–300	300–350	350–400	400–500	500–600	600–700
	EM7	EM8	EM9	EM10	EM11	EM12	
	700–800	800–900	900–1000	1000–1100	1100–1200	> 1200	
Inclusive (IM)	IM0	IM1	IM2	IM3	IM4	IM5	IM6
$E_{\mathrm{T}}^{\mathrm{miss}}$ [GeV]	> 200	> 250	> 300	> 350	> 400	> 500	> 600
	IM7	IM8	IM9	IM10	IM11	IM12	
	> 700	> 800	> 900	> 1000	> 1100	> 1200	

calorimeter layer, and the charged-particle fraction.[2] Loose selection criteria are applied to all jets with $p_{\mathrm{T}} > 30\,\mathrm{GeV}$ and $|\eta| < 2.8$, which remove anomalous energy depositions due to coherent noise and electronic noise bursts in the calorimeter [102]. Events with any jet not satisfying the loose criteria [101] are discarded.

Non-collision backgrounds, for example energy depositions in the calorimeters due to muons of beam-induced or cosmic-ray origin, are suppressed by imposing tight selection criteria on the leading jet: the ratio of the jet charged-particle fraction to the maximum fraction of the jet energy collected by a single calorimeter layer, $f_{\mathrm{ch}}/f_{\mathrm{max}}$, is required to be larger than 0.1. Jet quality requirements altogether have a negligible effect on the signal efficiency.

The signal region (SR) is divided in different bins of $E_{\mathrm{T}}^{\mathrm{miss}}$, which are listed in Table 1. Inclusive bins are used for a model-independent interpretation of search results, while the full set of exclusive bins are used for the interpretation within different models of new physics.

6 Background estimation

A semi-data-driven technique, supported by statistically-independent control regions, is used to constrain the normalization of Standard Model backgrounds. The approach followed is similar to the one of the previous versions of the analysis [1].

6.1 Control regions

The estimation of the Z + jets, W + jets, $t\bar{t}$, and single-t backgrounds is performed using five control regions, as described below. These regions are defined in a way similar to the SR: after applying the same selection criteria on jet multiplicity and azimuthal separation with $E_{\mathrm{T}}^{\mathrm{miss}}$, as well as on the leading jet p_{T}, events are selected in terms of a quantity which – as $E_{\mathrm{T}}^{\mathrm{miss}}$ does in the SR – is a proxy for the transverse momentum of the system which recoils against the hadronic activity in the event. This quantity is denoted in the following as $p_{\mathrm{T}}^{\mathrm{recoil}}$. Control regions are binned in terms of $p_{\mathrm{T}}^{\mathrm{recoil}}$, using the same binning as in the signal region (see Table 1). In the signal region, $p_{\mathrm{T}}^{\mathrm{recoil}}$ is equivalent to $E_{\mathrm{T}}^{\mathrm{miss}}$.

A control region enriched in $W \to \mu\nu$ events is defined by selecting events that pass the same trigger requirements as in the signal region, if they have exactly one reconstructed muon and this muon has

[2] The charged-particle fraction is defined as $f_{\mathrm{ch}} = \sum p_{\mathrm{T}}^{\mathrm{track,jet}}/p_{\mathrm{T}}^{\mathrm{jet}}$, where $\sum p_{\mathrm{T}}^{\mathrm{track,jet}}$ is the scalar sum of the transverse momenta of tracks associated with the primary vertex within a cone of radius $\Delta R = 0.4$ around the jet axis, and $p_{\mathrm{T}}^{\mathrm{jet}}$ is the transverse momentum of the jet as determined from calorimetric measurements.

$p_{\mathrm{T}} > 10\,\mathrm{GeV}$ and passes requirements on the transverse and longitudinal impact parameters, and if no electrons, τ-leptons, photons or b-jets are reconstructed. In this region, $p_{\mathrm{T}}^{\mathrm{recoil}}$ is defined as the magnitude of the vector sum of the missing transverse momentum and of the muon transverse momentum, $|\mathbf{p}_{\mathrm{T}}^{\mathrm{miss}} + \mathbf{p}_{\mathrm{T}}(\mu)|$, and is required to be higher than 200 GeV. An additional requirement on the transverse mass is applied, $30\,\mathrm{GeV} < m_{\mathrm{T}} < 100\,\mathrm{GeV}$, where $m_{\mathrm{T}} = \sqrt{2p_{\mathrm{T}}(\mu)p_{\mathrm{T}}(\nu)(1-\cos(\Delta\phi(\mu,\nu))}$ and the neutrino transverse momentum, $\mathbf{p}_{\mathrm{T}}(\nu)$, is taken to be the same as $\mathbf{p}_{\mathrm{T}}^{\mathrm{miss}}$.

Similarly, a control region enriched in $Z \to \mu\mu$ events is defined by selecting events that pass the same trigger requirements but have exactly two reconstructed muons, where these muons have $p_{\mathrm{T}} > 10\,\mathrm{GeV}$ and pass requirements on the transverse and longitudinal impact parameters, and the invariant mass of the di-muon system is between 66 and 116 GeV. In this region, $p_{\mathrm{T}}^{\mathrm{recoil}}$ is defined as the magnitude of the vector sum of the missing transverse momentum and the transverse momentum of the di-muon system, $|\mathbf{p}_{\mathrm{T}}^{\mathrm{miss}} + \mathbf{p}_{\mathrm{T}}(\mu\mu)|$, and is required to be higher than 200 GeV. The trigger requirements used for these two regions do not include muon information in the calculation of $E_{\mathrm{T}}^{\mathrm{miss}}$, and are fully efficient for events passing the selection criteria.

A control region enriched in $W \to e\nu$ events is defined by selecting events that pass single-electron triggers, if they have exactly one reconstructed electron and this electron passes tight identification criteria described in Ref. [97], is reconstructed outside the transition region between the EM barrel and endcap calorimeters, has $p_{\mathrm{T}} > 30\,\mathrm{GeV}$ and passes the tight isolation requirements based on information from the EM calorimeter and from tracking detectors, described in Ref. [93]. In this region, $p_{\mathrm{T}}^{\mathrm{recoil}}$ is defined as the magnitude of the vector sum of the missing transverse momentum and of the electron transverse momentum, $|\mathbf{p}_{\mathrm{T}}^{\mathrm{miss}} + \mathbf{p}_{\mathrm{T}}(e)|$, and is required to be higher than 200 GeV. The transverse mass is required to be $30\,\mathrm{GeV} < m_{\mathrm{T}} < 100\,\mathrm{GeV}$.

Similarly, a control region enriched in $Z \to ee$ events is defined by selecting events with exactly two reconstructed electrons, where these electrons have $p_{\mathrm{T}} > 30\,\mathrm{GeV}$ and the invariant mass of the di-electron system is between 66 and 116 GeV. In this region, $p_{\mathrm{T}}^{\mathrm{recoil}}$ is defined as the magnitude of the vector sum of the missing transverse momentum and of the transverse momentum of the di-electron system, $|\mathbf{p}_{\mathrm{T}}^{\mathrm{miss}} + \mathbf{p}_{\mathrm{T}}(ee)|$, and is required to be higher than 200 GeV. The single-electron trigger requirements are fully efficient for events passing the selection criteria of these two regions.

A control region enriched in $t\bar{t}$ and single-t events is defined by selecting events which pass the same cuts of the $W \to \mu\nu$ and $W \to e\nu$ regions, but which have at least one identified b-jet.

Table 2 shows a summary of the selection criteria for all regions.

6.2 Multi-jet background

The multi-jet background with large $E_{\mathrm{T}}^{\mathrm{miss}}$ mainly originates from the mis-reconstruction of the energy of a jet in the calorimeter and, to a lesser extent, is due to the presence of neutrinos in the final state from heavy-flavour hadron decays. In this analysis, the multi-jet background is determined from data, using the jet smearing method as described in Ref. [103]. It relies on the assumption that the $E_{\mathrm{T}}^{\mathrm{miss}}$ value of multi-jet events is dominated by fluctuations in the jet response in the detector, which can be measured in the data. The method was validated with data from a control region where events were selected as in the signal region, except for a modified requirement that the minimum azimuthal distance between a jet and $\mathbf{p}_{\mathrm{T}}^{\mathrm{miss}}$ is between 0.3 and 0.4. After event selection, the multi-jet background constitutes about 1.2%, 0.8%, 0.4% and 0.3% of the total background in the exclusive bins EM1, EM2, EM3 and EM4, respectively,

Table 2: Event selection criteria for the signal and control regions. Reconstructed objects are defined as explained in Sec. 4.

Requirement	**SR**	$W \to \mu\nu$	$Z \to \mu\mu$	$W \to e\nu$	$Z \to ee$	**top**
primary vertex	at least one with ≥ 2 associated tracks with $p_{\mathrm{T}} > 500\,\mathrm{MeV}$					
trigger	$E_{\mathrm{T}}^{\mathrm{miss}}$			single-electron		$E_{\mathrm{T}}^{\mathrm{miss}}$, single-electron
$p_{\mathrm{T}}^{\mathrm{recoil}}$ cut	$E_{\mathrm{T}}^{\mathrm{miss}} > 200\,\mathrm{GeV}$	$\lvert\mathbf{p}_{\mathrm{T}}^{\mathrm{miss}} + \mathbf{p}_{\mathrm{T}}(\mu)\rvert > 200\,\mathrm{GeV}$	$\lvert\mathbf{p}_{\mathrm{T}}^{\mathrm{miss}} + \mathbf{p}_{\mathrm{T}}(\mu\mu)\rvert > 200\,\mathrm{GeV}$	$\lvert\mathbf{p}_{\mathrm{T}}^{\mathrm{miss}} + \mathbf{p}_{\mathrm{T}}(e)\rvert > 200\,\mathrm{GeV}$	$\lvert\mathbf{p}_{\mathrm{T}}^{\mathrm{miss}} + \mathbf{p}_{\mathrm{T}}(ee)\rvert > 200\,\mathrm{GeV}$	$\lvert\mathbf{p}_{\mathrm{T}}^{\mathrm{miss}} + \mathbf{p}_{\mathrm{T}}(\mu)\rvert > 200\,\mathrm{GeV}$ or $\lvert\mathbf{p}_{\mathrm{T}}^{\mathrm{miss}} + \mathbf{p}_{\mathrm{T}}(e)\rvert > 200\,\mathrm{GeV}$
jets	up to 4 with $p_{\mathrm{T}} > 30\,\mathrm{GeV}$, $\lvert\eta\rvert < 2.8$					
$\lvert\Delta\phi(\mathrm{jets}, \mathbf{p}_{\mathrm{T}}^{\mathrm{miss}})\rvert$	> 0.4 (> 0.6 if $200\,\mathrm{GeV} < E_{\mathrm{T}}^{\mathrm{miss}} \leq 250\,\mathrm{GeV}$)					
leading jet	$p_{\mathrm{T}} > 150\,\mathrm{GeV}$, $\lvert\eta\rvert < 2.4$, $f_{\mathrm{ch}}/f_{\mathrm{max}} > 0.1$					
b-jets	any	none	any	none	any	at least one
electrons or muons	none	exactly one muon, with $p_{\mathrm{T}} > 10\,\mathrm{GeV}$, $30 < m_{\mathrm{T}} < 100\,\mathrm{GeV}$; no electron	exactly two muons, with $p_{\mathrm{T}} > 10\,\mathrm{GeV}$, $66 < m_{\mu\mu} < 116\,\mathrm{GeV}$; no electron	exactly one electron, tight, with $p_{\mathrm{T}} > 30\,\mathrm{GeV}$, $\lvert\eta\rvert \notin (1.37, 1.52)$, tight isolation, $30 < m_{\mathrm{T}} < 100\,\mathrm{GeV}$; no muon	exactly two electrons, with $p_{\mathrm{T}} > 30\,\mathrm{GeV}$, $66 < m_{ee} < 116\,\mathrm{GeV}$; no muon	as for $W \to \mu\nu$ or as for $W \to e\nu$
τ-leptons	none					
photons	none					

and it is negligible for the other signal region bins. A conservative 100% uncertainty is assigned on the normalization of this background .

6.3 Non-collision background

After event selections are applied, the signal region may contain residual contributions from non-collision backgrounds. These backgrounds mainly arise when beam-halo protons intercept the LHC collimators, leading to particle cascades which produce muons. The remaining contributions are estimated following the methods set out in [102]. In particular, the jet timing, t_j, calculated from the energy-weighted average of the time of the jet energy deposits, defined with respect to the event time in nominal collisions, is used. A dedicated region enhanced in beam-induced background, defined by inverting the tight jet-quality selection imposed on the leading jet, is used to estimate the amount of non-collision background from the fraction of events with a leading-jet timing $|t_j| > 5\,\mathrm{ns}$. The results indicate a negligible contribution, at the per mille level, from non-collision backgrounds in the signal region. A conservative 100% uncertainty is assigned to the normalization of this background.

6.4 Standard Model background fit

The estimation of backgrounds in the SR is based on a simultaneous, binned likelihood fit to the $p_{\mathrm{T}}^{\mathrm{recoil}}$ distribution of the five control regions described in Section 6.1. The number of events in each region and in each bin is treated as a random variable with a Poisson distribution function, with an expectation value given by the sum of the SM predictions for each background in that bin. The likelihood fit is based on the profile likelihood method [104]. Systematic uncertainties are represented by Gaussian-distributed nuisance parameters, and take into account the correlation among systematic variations and across $p_{\mathrm{T}}^{\mathrm{recoil}}$ bins.

The normalization of all W + jets and Z + jets processes, excluding those initiated by VBF, is multiplied by a single floating normalization factor, which is the same across all $p_{\mathrm{T}}^{\mathrm{recoil}}$ bins. As a result, data from both W and Z control regions are used simultaneously to constrain the $Z \to \nu\nu$ background in the signal region. Systematic uncertainties on W + jets and Z + jets, as described in Sec. 7, cover the residual bin-by-bin differences among processes when higher-order calculations are included, taking into account the correlation of theoretical uncertainties across different processes with the calculation provided in Ref. [79]. Similarly, one floating normalization factor is used for each of the $t\bar{t}$ and single-t backgrounds, resulting in a total of three floating background normalization factors in the fit. With respect to the previous version of the analysis, the usage of two independent normalization factors for the two main sources of top quark backgrounds was introduced to better take into account their different expected contribution as a function of $p_{\mathrm{T}}^{\mathrm{recoil}}$.

Table 3 shows the results of the background-only fit to the control regions, when all exclusive bins are fitted simultaneously. The normalizations of the W + jets and Z + jets backgrounds get corrected by a multiplicative factor of 1.14 ± 0.01, while the normalization of the $t\bar{t}$ and single-t backgrounds gets corrected by a multiplicative factor of 0.9 ± 0.1 and 1.5 ± 0.4, respectively.

Figures 2 and 3 show the expected and observed distribution of the $p_{\mathrm{T}}^{\mathrm{recoil}}$ in the control regions. The shown expected distributions include the data-driven normalization factors as extracted from the binned likelihood fit to the different exclusive $p_{\mathrm{T}}^{\mathrm{recoil}}$ bins in the control regions. Good agreement is observed, within statistical and systematic uncertainties, with data. As illustration, χ^2-statistical tests, using the binned profile likelihood fit described above, probing potential shape discrepancies in the observed and predicted $p_{\mathrm{T}}^{\mathrm{recoil}}$ distributions, gives p-values in the range between 0.49 (in the $Z \to ee$ control region) to 0.99 (in the top quark control region).

In order to perform model-independent tests of new physics processes, discussed in Sec. 8.1, the same fit procedure is repeated in each of the inclusive bins of $p_{\mathrm{T}}^{\mathrm{recoil}}$ for signal and control regions, denoted in Table 1 as IM0-IM12. Since in this case no shape information is available to constrain the separate contributions of $t\bar{t}$ and single-t, a single normalization factor is used for all top-quark-related processes, along with the normalization factor for W/Z+jets, resulting in two free background normalization factors in the fit. Additionally, the nuisance parameters related to systematic uncertainties refer to the given $E_{\mathrm{T}}^{\mathrm{miss}}$ inclusive region. A total of 13 separate fits is therefore performed, based on five control regions each and including two free background normalization factors. Different results are expected with respect to the simultaneous fit to exclusive bins, due to the lack of information from the $p_{\mathrm{T}}^{\mathrm{recoil}}$ shape information which cannot be used to constrain uncertainties and the normalization of backgrounds.

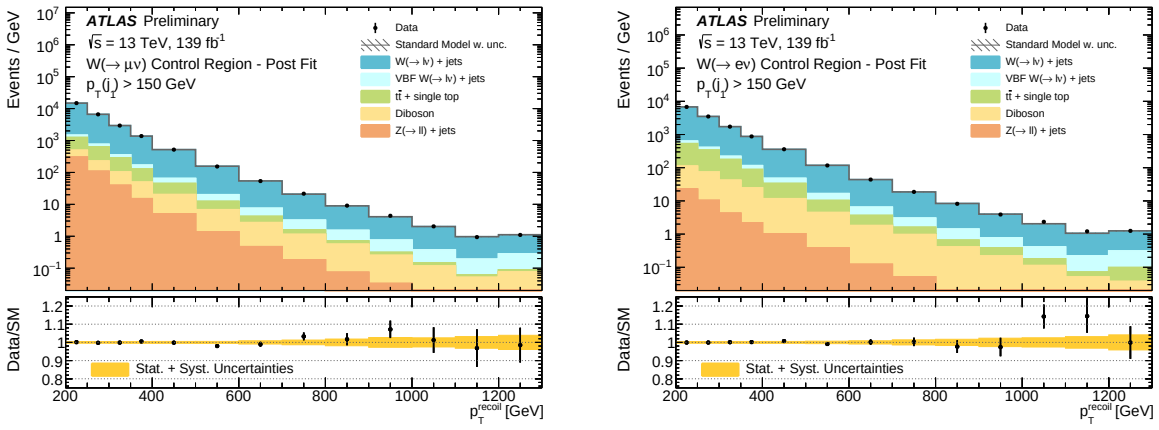

(a)

(b)

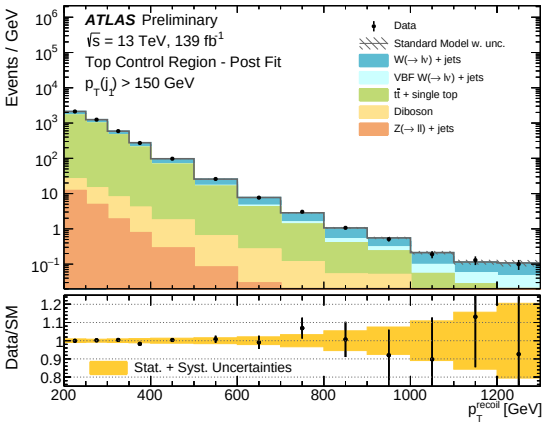

(a)

(c)

Figure 2: The measured distributions in the (a) $W \to \mu\nu$, (b)$W \to e\nu$ and (c) top control regions, compared to the background predictions as estimated after the simultaneous, binned background-only fit to the data in the control regions. The error bands in the ratios include the statistical and systematic uncertainties in the background predictions. Events with values beyond the range of the histogram are included in the last bin.

Table 3: Expected and observed events with $p_{\mathrm{T}}^{\mathrm{recoil}} > 200\,\mathrm{GeV}$ in the five control regions (top: post-fit, bottom: pre-fit). The post-fit predictions for the SM backgrounds are obtained after the simultaneous binned likelihood fit to the five control regions, performed in the exclusive bins of $p_{\mathrm{T}}^{\mathrm{recoil}}$ (EM0–EM12). The background predictions include both the statistical and systematic uncertainties. The individual uncertainties are correlated, and do not necessarily add in quadrature to the total background uncertainty. The dash '–" denotes negligible contributions.

$\mathbf{p_T^{recoil} > 200\,GeV}$	$W \to \mu\nu$	$W \to e\nu$	Top	$Z \to \mu\mu$	$Z \to ee$
Observed events ($139\,\mathrm{fb}^{-1}$)	1364958	699674	225606	196800	145531
SM prediction (post-fit)	1365000 ± 6000	699700 ± 3300	225600 ± 2100	196930 ± 1000	145500 ± 800
Fitted $W \to e\nu$	46.0 ± 1.6	579000 ± 4000	16100 ± 800	–	70.3 ± 2.4
Fitted $W \to \mu\nu$	1147000 ± 8000	51.4 ± 1.8	31400 ± 1700	222 ± 8	–
Fitted $W \to \tau\nu$	70900 ± 800	45100 ± 500	3340 ± 180	20.5 ± 0.8	4.55 ± 0.18
Fitted $VBFW$ + jets	26600 ± 2900	14600 ± 1700	2050 ± 340	4.07 ± 0.07	2.36 ± 0.04
Fitted $Z \to ee$	–	232 ± 8	7.14 ± 0.24	–	137900 ± 900
Fitted $Z \to \mu\mu$	21100 ± 600	0.84 ± 0.03	780 ± 27	184800 ± 1200	–
Fitted $Z \to \tau\tau$	2660 ± 100	1890 ± 70	234 ± 9	118 ± 4	109 ± 4
Fitted $Z \to \nu\nu$	358 ± 12	13.8 ± 0.5	57.7 ± 2.0	0.051 ± 0.002	–
Fitted $VBFZ$ + jets	242 ± 4	29.0 ± 0.5	10.72 ± 0.18	3400 ± 400	2600 ± 300
Fitted single-t	21000 ± 6000	12700 ± 3300	32000 ± 9000	340 ± 160	110 ± 60
Fitted $t\bar{t}$	52000 ± 4000	34200 ± 2500	138000 ± 7000	4100 ± 300	1820 ± 160
Expected dibosons	23000 ± 4000	12400 ± 2100	1900 ± 400	4000 ± 700	2900 ± 500
MC exp. SM events	1220000 ± 60000	623000 ± 32000	233000 ± 30000	175000 ± 9000	128000 ± 8000
Fit input $W \to e\nu$	40.8 ± 0.7	509000 ± 27000	14200 ± 1200	–	62.4 ± 1.1
Fit input $W \to \mu\nu$	1010000 ± 50000	45.6 ± 0.8	28000 ± 2300	197.0 ± 3.3	–
Fit input $W \to \tau\nu$	63000 ± 3300	39800 ± 2100	2970 ± 250	18.17 ± 0.31	4.07 ± 0.07
Fit input $VBFW$ + jets	22000 ± 4000	11700 ± 2300	1500 ± 400	4.07 ± 0.07	2.36 ± 0.04
Fit input $Z \to ee$	–	205.5 ± 3.5	6.33 ± 0.11	–	120000 ± 7000
Fit input $Z \to \mu\mu$	18900 ± 1100	0.74 ± 0.01	689 ± 12	163000 ± 9000	–
Fit input $Z \to \tau\tau$	2355 ± 40	1680 ± 29	207.2 ± 3.5	105.0 ± 1.8	96.4 ± 1.6
Fit input $Z \to \nu\nu$	318 ± 5	12.2 ± 0.2	51.2 ± 0.9	–	–
Fit input $VBFZ$ + jets	243 ± 4	29.0 ± 0.5	10.70 ± 0.18	2700 ± 500	2000 ± 400
Fit input single-t	16000 ± 6000	10000 ± 4000	28000 ± 12000	700 ± 500	280 ± 200
Fit input $t\bar{t}$	60000 ± 7000	39000 ± 5000	155000 ± 27000	4600 ± 1300	2000 ± 700
Fit input dibosons	23000 ± 5000	12600 ± 2300	1900 ± 400	4100 ± 800	3000 ± 600

7 Systematic uncertainties

The impact of systematic uncertainties is estimated after performing a background-only fit to exclusive CR data, and evaluating the impact of the uncertainty in the total background yield in each bin of $p_{\mathrm{T}}^{\mathrm{recoil}}$ in the SR. The dominant sources of experimental uncertainty are those related to the electron, muon and jet identification and reconstruction efficiencies, while uncertainties on the V + jets predictions give the leading contribution to theory uncertainties. More details are provided in the following sections.

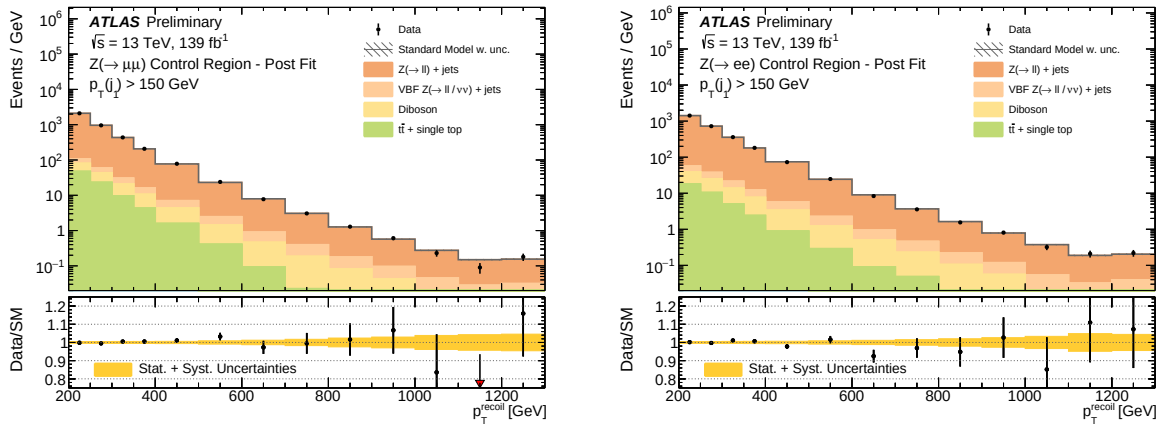

(a) (b)

Figure 3: The measured $p_{\mathrm{T}}^{\mathrm{recoil}}$ distributions in the (a) $Z \to \mu\mu$ and (b) $Z \to ee$ control regions, compared to the background predictions as estimated after the simultaneous, binned background-only fit to the data in the control regions. The error bands in the ratios include the statistical and systematic uncertainties in the background predictions. Events with values beyond the range of the histogram are included in the last bin.

7.1 Background uncertainties

The uncertainty in the combined 2015-2018 integrated luminosity is 1.7%. It is derived from the calibration of the luminosity scale using x-y beam-separation scans, following a methodology similar to that described in Ref. [105], and using the LUCID-2 detector for the baseline luminosity measurements [106]. This uncertainty nearly cancels in the semi-data-driven background estimation procedure, and translates into a residual uncertainty on the total SR background of less than 0.01% (0.1%) for $p_{\mathrm{T}}^{\mathrm{recoil}} = 200\,\mathrm{GeV}$ (1200 GeV). The uncertainty on the pile-up reweighting procedure translates into a residual uncertainty on the total SR background of less than 0.5% (0.2%) for $p_{\mathrm{T}}^{\mathrm{recoil}} = 200\,\mathrm{GeV}$ (1200 GeV).

Systematic uncertainties in the jet energy scale and resolution [88, 107] and in the modelling of the JVT requirement used to reject jets coming from pileup [108] translate into uncertainties in the total background in the SR which vary between 0.3% and 1.4% for $p_{\mathrm{T}}^{\mathrm{recoil}}$ between 200 GeV and 1200 GeV. Uncertainties in the flavour tagging efficiency [109] translate into uncertainties in the total background in the SR between 0.1% and 1% for $p_{\mathrm{T}}^{\mathrm{recoil}}$ between 200 GeV and 1200 GeV.

Uncertainties in the $E_{\mathrm{T}}^{\mathrm{miss}}$ scale (resolution) due to soft contributions to the $E_{\mathrm{T}}^{\mathrm{miss}}$ calculation translate into uncertainties in the total background in the SR between 0.5% (0.3%) and 0.3% (0.1%) for $p_{\mathrm{T}}^{\mathrm{recoil}}$ between 200 GeV and 1200 GeV.

Uncertainties in the electron reconstruction and identification efficiencies [110] and in the electron and photon energy scale and resolution [111] translate into uncertainties in the total background in the SR between 0.7% and 2.3% for $p_{\mathrm{T}}^{\mathrm{recoil}}$ between 200 GeV and 1200 GeV. Uncertainties due to electron trigger and isolation efficiencies give a contribution of less than 0.1% across the $p_{\mathrm{T}}^{\mathrm{recoil}}$ spectrum. Negligible contributions are given by the photon identification efficiency. Uncertainties in the muon reconstruction and identification efficiencies and in their momentum scale and resolution [94] translate into uncertainties in the total background in the SR between 0.6% and 2.2% for $p_{\mathrm{T}}^{\mathrm{recoil}}$ between 200 GeV and 1200 GeV. Uncertainties in the τ-lepton reconstruction and identification efficiencies translate into uncertainties in the total background in the SR of 0.1% (0.03%) for $p_{\mathrm{T}}^{\mathrm{recoil}} = 200\,\mathrm{GeV}$ ($> 1200\,\mathrm{GeV}$).

Uncertainties on the higher-order QCD and electroweak parton-level calculations used to correct the MC prediction for V + jets processes not initiated by VBF are calculated following the procedure described in Ref. [79]. These uncertainties, which are treated as correlated across $p_{\mathrm{T}}^{\mathrm{recoil}}$ bins and – unless otherwise noted – as correlated across processes, include: uncertainties in the QCD renormalization and factorization scales; uncertainties associated with the non-universality of QCD corrections across W + jets and Z + jets processes; uncertainties in electroweak corrections beyond NNLO, unknown electroweak NLO correction terms at very high boson-p_{T} (uncorrelated across processes), and limitations of the Sudakov approximation adopted in the calculation (uncorrelated across processes); uncertainties in the QCD and electroweak interference terms; and uncertainties on the parton distribution functions. In particular, the sum in quadrature was considered for the latter, following Eq. 20 of Ref. [112] and keeping the correlation of the individual sets between the different processes. Overall, these translate in uncertainties in the total background in the SR between 0.4% and 2% for $p_{\mathrm{T}}^{\mathrm{recoil}}$ between 200 GeV and 1200 GeV, with the leading contributions given by QCD and electroweak uncertainties, respectively. An additional systematic uncertainty is included to cover for possible differences in the definition of τ-leptons at truth Monte Carlo level with respect to the one used in the theoretical calculation from Ref. [79], which translates in uncertainties in the total background in the SR between 0.05% and 0.1% for $p_{\mathrm{T}}^{\mathrm{recoil}}$ between 200 GeV and 1200 GeV.

Uncertainties on the V + jets processes initiated by VBF include scale and PDF uncertainties and the comparison with Sherpa as an alternative MC generator. They translate in uncertainties in the total background in the SR between 0.02% and 0.1% for $p_{\mathrm{T}}^{\mathrm{recoil}}$ between 200 GeV and 900 GeV, and between 0.4% and 1.4% for $p_{\mathrm{T}}^{\mathrm{recoil}}$ between 1000 GeV and 1200 GeV.

Uncertainties on the theoretical predictions of the $t\bar{t}$ and single-t backgrounds are estimated separately for the two processes by varying parton-shower parameters and the amount of initial- and final-state soft gluon radiation, by comparing predictions from different MC event generators [113] and by evaluating the interference between single-t in the Wt-channel and $t\bar{t}$ comparing the DR and DS schemes described in Ref. [114]. In the case of $t\bar{t}$ (single-t), they translate in uncertainties in the total background in the SR between 0.2% (0.2%) and 0.7% (0.4%) for $p_{\mathrm{T}}^{\mathrm{recoil}}$ between 200 GeV and 1200 GeV.

Uncertainties on the theoretical predictions of diboson backgrounds include a 6% theory uncertainty in the NLO cross section, as well as uncertainties in the QCD renormalization, factorization and resummation scales, uncertainties due to the choice of the parton distribution functions and uncertainties on the modelling of the parton showers. They translate in uncertainties in the total background in the SR between 0.05% and 0.2% for $p_{\mathrm{T}}^{\mathrm{recoil}}$ between 200 GeV and 1200 GeV.

Uncertainties in the multi-jet and non-collision backgrounds translate in uncertainties in the total background in the SR for $p_{\mathrm{T}}^{\mathrm{recoil}} = 200$ GeV of 1% and 0.2%, respectively, and are negligible above 800 GeV.

7.2 Signal uncertainties

Sources of systematic uncertainty in the predicted signal yields are considered separately for each model of new physics using a common set of procedures. Experimental uncertainties include those related to the jet and $E_{\mathrm{T}}^{\mathrm{miss}}$ reconstruction, energy scales and resolutions, which introduce uncertainties in the signal yields for the different models that vary in the range between 1% and 3% at low $p_{\mathrm{T}}^{\mathrm{recoil}}$, and between 4% and 7% at large $p_{\mathrm{T}}^{\mathrm{recoil}}$, depending on the parameters of the model. The 1.7% uncertainty on the integrated luminosity is also included. Other uncertainties related to the jet quality requirements are negligible.

Uncertainties affecting the signal acceptance in the generation of signal samples include: uncertainties in the modelling of the initial- and final-state radiation and the underlying event, determined using simulated samples with modified parton-shower parameters (by factors of two or one half); uncertainties due to PDFs and variations of the $\alpha_s(m_Z)$ value employed, as computed from the envelope of CT10 or CT14, MMHT2014 [115] and NNPDF30 error sets; and uncertainties due to the choice of renormalization and factorization scales, which are varied by factors of two or one half. In addition, theoretical uncertainties in the predicted cross sections, including PDF and renormalization- and factorization-scale uncertainties, are assessed and their effect is shown in terms of variations of the observed results.

In the case of WIMP production models, the uncertainty related to the modelling of the initial- and final-state radiation translates into a 3% to 6% uncertainty in the signal acceptance. The choice of different PDF sets results in up to a 10% and a 20% uncertainty in the case of axial-vector and pseudoscalar models, respectively. Varying the renormalization and factorization scales introduces a 0.1% to 21% variations in the signal acceptance, depending on the model and the mediator and WIMP masses considered. Renormalization and factorization scale uncertainties introduce an uncertainty in the cross section predictions of about 10% in the case of the axial-vector mediator model and up to 50% for the pseudoscalar mediator model. Finally, PDF uncertainties translate into cross section uncertainties of about 5% and 20% for the axial-vector and pseudoscalar mediator models, respectively.

Similarly, for SUSY models, the uncertainties related to the modelling of initial- and final-state gluon radiation and the matching between matrix elements and parton showers in the simulation translate into a 7% to 8% uncertainty in the signal acceptance. Variations of the renormalization and factorization scales introduce an about 3% uncertainty in the signal acceptance. Uncertainties on the predicted cross sections, including both renormalization/factorization scale and PDF uncertainties, increase with squark masses in the range between 7%, for a mass of 100 GeV, and about 11% of a mass of about 1 TeV.

In the case of dark energy inspired models, uncertainties related to renormalization/factorization scales, PDFs, and parton shower modelling vary the signal acceptance by 0.1% to 3.5%, 1% to 16%, and 0.1% to 5%, respectively, with increasing $E_{\mathrm{T}}^{\mathrm{miss}}$. Renormalization/factorization scale and PDF uncertainties introduce uncertainties in the cross section predictions of about 30% each.

For the ADD model, the uncertainties related to the modelling of the initial- and final-state gluon radiation translate into uncertainties in the ADD signal acceptance which vary between 11% and 13% with increasing $E_{\mathrm{T}}^{\mathrm{miss}}$ and approximately independent of n. The uncertainties due to the PDFs, affecting both signal normalization and acceptance, increase from 11% at $n = 2$ to 43% at $n = 6$. Similarly, the variations of the renormalization and factorization scales introduce a 23% to 36% uncertainty in the signal yields, with increasing n.

For the ALPs production model, theoretical uncertainties related to PDFs, affecting signal normalization and acceptance, translate into uncertainties in the signal yields that vary in the range between 2% and 14%. Variations of the renormalization and factorization scales and matrix elements to parton shower matching scales, introduce uncertainties in the signal yields that vary between 5% and 50%. Variations in the parton-shower modelling translate into uncertainties on the signal acceptance in the range between 1% and 20%, depending on the $E_{\mathrm{T}}^{\mathrm{miss}}$ bin considered.

Finally, for the interpretation of an invisibly decaying Higgs boson, uncertainties related to PDFs, affecting both signal normalization and signal acceptance, translate into 1% to 5% variations in the Higgs signal yields as $E_{\mathrm{T}}^{\mathrm{miss}}$ increases. Variations in the renormalization and factorization scales introduce a 15% uncertainty in the signal yields. Uncertainties in the parton shower modelling translate into uncertainties in the signal acceptance that vary between 12% and 40% with increasing $E_{\mathrm{T}}^{\mathrm{miss}}$. Uncertainties in the higher-order

Table 4: Data and SM background predictions in the signal region for several inclusive $p_{\mathrm{T}}^{\mathrm{recoil}}$ selections, as determined using separate one-bin likelihood fits in the control regions. For the SM prediction, both the statistical and systematic uncertainties are included. In each signal region, the individual uncertainties for the different background processes can be correlated, and do not necessarily add in quadrature to the total background uncertainty. The dash "–" denotes negligible background contributions. For illustration, the expected events yields for particular signals for new phenomena are provided.

Inclusive Signal Region	IM1	IM3	IM5	IM7	IM10	IM12
Observed events (139 fb^{-1})	1357019	290779	46855	7194	807	207
SM prediction	1340000 ± 16000	285000±4000	45200±900	6990±230	710±50	221±18
$W \to e\nu$	70700±2000	11800±400	1390±70	167±12	12.1±1.4	2.8±0.4
$W \to \mu\nu$	105400±2300	17500±400	2220±70	304±14	37±4	14.6±1.7
$W \to \tau\nu$	243000±4000	44800±800	5880±160	790±40	65±6	17.6±2.0
$VBFW$ + jets	7900±1600	2200±600	450±150	80±40	9±8	3.8±3.5
$Z \to ee$	–	–	–	–	–	
$Z \to \mu\mu$	2950±140	313±15	24.8±1.4	5.5±0.4	1.54±0.19	1.28±0.18
$Z \to \tau\tau$	2540±120	355±18	42.7±2.4	7.5±0.6	2.73±0.33	0.5±0.1
$Z \to \nu\nu$	813000±10000	189000±4000	32100±900	5090±240	510±50	157±18
$VBFZ$ + jets	13600±2800	4800±1100	1210±350	260±90	35±14	13±6
$t\bar{t}$ and single-t	46700±2000	6899±400	600±70	45±15	–	–
Diboson	26000±5000	7700±1500	1600±400	310±80	38±12	13±4
Multijet	7000±7000	450±450	5.3±5.3	0.2±0.2	–	–
Non-collision background	1200±1200	162±162	29±29	6±6	–	–
SUSY, m($\tilde{t}$, $\tilde{\chi}^0$) = (600, 580) GeV	2130±40	1155±23	354±11	107±5	62.2±3.0	19.1±1.0
DMA, m(χ, M$_{Z_A}$) = (1, 2000)	3970±110	2150±70	920±40	335±16	82±6	35±3
Dark Energy, M$_2$ = 1558 GeV	953±16	600±10	247±5	105±3	69.4±2.1	30.8±1.2

electroweak corrections, especially relevant for VBF and VH processes, translate into uncertainties on the signal yield in the range between 15% and 60% with increasing $E_{\mathrm{T}}^{\mathrm{miss}}$.

8 Results and interpretations

Figure 4 shows several measured distributions in the signal region compared to the SM predictions obtained from the fit to CRs. As discussed in Section 6, the SM predictions are normalized with normalization factors determined from the global fit carried out in exclusive $p_{\mathrm{T}}^{\mathrm{recoil}}$ bins. The fitting procedure also constrains the background uncertainties resulting in a precise SM prediction in almost the whole $p_{\mathrm{T}}^{\mathrm{recoil}}$ spectrum. As an example, the SM predictions are determined with a total uncertainty of 1.5%, 1.2%, and 4.1% for the EM0, EM4, and EM12 signal regions, respectively, which include correlations between uncertainties in the individual background contributions.

The number of events in the data and the individual background predictions are presented in Tables 4 and 5 for inclusive and exclusive $p_{\mathrm{T}}^{\mathrm{recoil}}$ bins, respectively. The results for all the signal regions are summarized in Table 6. An overall good agreement between data and SM predictions is observed although a slight excess (at the level of 1.5σ) in the region $600 < p_{\mathrm{T}}^{\mathrm{recoil}} < 800$ GeV is noted. The compatibility of the data with a SM background hypothesis is tested using a χ^2-statistical test and the binned profile likelihood fit described above. The resulting statistical tests for a background-only hypothesis, in the presence of different potential signal contributions, give p-values in the range between 0.009 and 1.0, where the minimum corresponds to a signal for stop-pair production in the $\tilde{t}_1 \to c + \tilde{\chi}_1^0$ decay channel with $m_{\tilde{t}_1} = 500$ GeVand $m_{\tilde{\chi}_1^0} = 420$ GeVan a deviation of about 2.35σ from the background-only hypothesis.

The results are translated into upper limits for the presence of new phenomena, using a simultaneous likelihood fit in both the control and signal regions, and the CL_{s} modified frequentist approach [116]. As

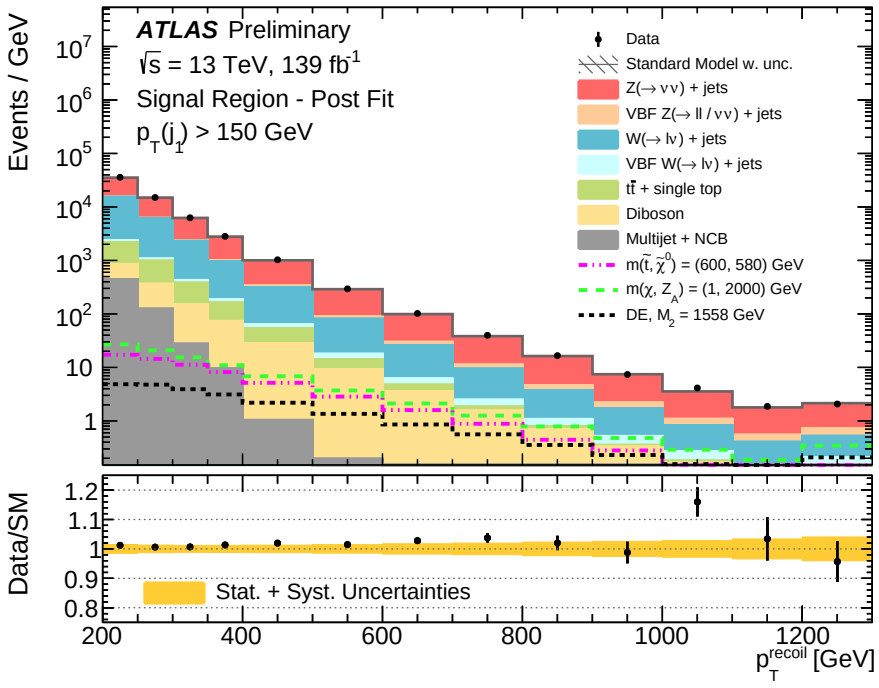

Figure 4: Measured distributions of $p_{\mathrm{T}}^{\mathrm{recoil}}$ for the $p_{\mathrm{T}}^{\mathrm{recoil}} > 200$ GeV selection compared to the SM predictions in the signal region. The latter are normalized with normalization factors as determined by the global fit that considers exclusive $p_{\mathrm{T}}^{\mathrm{recoil}}$ control regions. For illustration purposes, the distributions of examples of Dark Energy (DE), SUSY, and WIMP scenarios are included. The error band in the ratio shown in the lower panel includes both the statistical and systematic uncertainties in the background predictions. Events with values beyond the range of the histogram are included in the last bin.

already mentioned, inclusive regions with minimum $p_{\mathrm{T}}^{\mathrm{recoil}}$ thresholds are used to set model-independent exclusion limits, and the exclusive regions are used for the interpretation of the results within different models of new physics. For the latter, the presence of a slight excess of events at high $p_{\mathrm{T}}^{\mathrm{recoil}}$ limits the reach of the obtained observed limits, mostly for those models in which the expected signal would be accumulating at the tail of the $p_{\mathrm{T}}^{\mathrm{recoil}}$ distribution.

8.1 Model-independent exclusion limits

Results obtained in inclusive $p_{\mathrm{T}}^{\mathrm{recoil}}$ regions are translated into model-independent observed and expected 95% CL upper limits on the visible cross section, defined as the product of the production cross section, acceptance and efficiency $\sigma \times A \times \epsilon$. The limits are extracted from the ratio between the 95% CL upper limit on the number of signal events and the integrated luminosity, taking into consideration the systematic uncertainties in the SM backgrounds and the uncertainty in the integrated luminosity. A likelihood fit is performed separately for each of the inclusive regions IM0–IM12. The results are collected in Table 7. Values of $\sigma \times A \times \epsilon$ above 861 fb (for IM0) and above 0.3 fb (for IM12) are excluded at 95% CL.

Table 5: Data and SM background predictions in the signal region for several exclusive $p_{\mathrm{T}}^{\mathrm{recoil}}$ selections, as determined using a binned likelihood fit in the control regions. For the SM prediction, both the statistical and systematic uncertainties are included. In each signal region, the individual uncertainties for the different background processes can be correlated, and do not necessarily add in quadrature to the total background uncertainty. The dash "–" denotes negligible background contributions. For illustration, the expected event yields for particular signals for new phenomena are provided.

Exclusive Signal Region	EM2	EM4	EM6	EM8	EM9	EM11
Observed events (139 fb^{-1})	313912	102888	10203	1663	738	187
SM prediction	312000 ± 4000	100900±1200	9930±170	1630±40	747±19	181±6
$W \to e\nu$	15800±400	3890±100	274±10	35.0±1.6	13.11±0.6	2.93±0.16
$W \to \mu\nu$	23300±500	5880±120	475±12	65.8±2.2	30.7±1.2	7.7±0.4
$W \to \tau\nu$	54400±800	15310±260	1233±29	166±5	76.5±2.9	15.3±0.8
$VBFW$ + jets	2350±270	1019±140	142±26	29±7	16±5	5.3±1.9
$Z \to ee$	–	–	–	–	–	–
$Z \to \mu\mu$	596±20	97.5±3.3	4.52±0.16	1.49±0.05	0.60±0.02	–
$Z \to \tau\tau$	530±18	116±4	8.32±0.29	0.90±0.03	0.40±0.02	2.09±0.08
$Z \to \nu\nu$	191900±2200	67000±1000	6940±150	1170±40	527±19	124±6
$VBFZ$ + jets	3900±500	2210±290	380±60	88±17	47±10	14.4±3.4
$single-t$	2600±700	530±170	15±8	–	–	–
$t\bar{t}$	8900±500	2010±120	100±7	8.3±1.0	2.44±0.34	0.30±0.05
Diboson	6100±1000	2700±500	350±70	70±15	33±8	
Multijet	1130±1130	57±57	0.6±0.6	0.1±0.1	–	–
Non-collision background	243±243	46±46	8±8	6±6	–	–
SUSY, m($\tilde{t}$, $\tilde{\chi}^0$) = (600, 580) GeV	562±10	516±9	159±3	44.4±0.8	28.1±0.5	8.2±0.2
DMA, m(χ, M$_{Z_A}$) = (1, 2000)	770±20	684±20	212±8	79±4	47.9±2.5	18.7 ± 1.4
Dark Energy, M$_2$ = 1558 GeV	195±3	219±4	85.8±1.5	35.6±0.7	23.0±0.5	10.01±0.24

Table 6: Data and SM background predictions in the signal region for the different selections. For the SM predictions both the statistical and systematic uncertainties are included.

Inclusive Signal Region			**Exclusive Signal Region**		
Region	Predicted	Observed	Region	Predicted	Observed
IM0	3100000 ± 40000	3148643	EM0	1770000 ± 26000	1791624
IM1	1340000 ± 16000	1357019	EM1	747800 ± 10000	752328
IM2	596000 ± 7000	604691	EM2	312000 ± 4000	313912
IM3	285000 ± 4000	290779	EM3	139200 ± 1600	141036
IM4	146100 ± 2400	149743	EM4	100900 ± 1200	102888
IM5	45200 ± 900	46855	EM5	28999 ± 400	29458
IM6	16600 ± 500	17397	EM6	9930 ± 170	10203
IM7	6990 ± 230	7194	EM7	3840 ± 80	3986
IM8	3140 ± 120	3208	EM8	1630 ± 40	1663
IM9	1540 ± 70	1545	EM9	747 ± 19	738
IM10	710 ± 50	807	EM10	356 ± 10	413
IM11	390 ± 40	394	EM11	181 ± 6	187
IM12	221 ± 18	207	EM12	216 ± 9	207

8.2 Model-dependent exclusion limits

A simultaneous fit to the signal and control regions in the exclusive $p_{\mathrm{T}}^{\mathrm{recoil}}$ bins is performed, and used to set observed and expected 95% CL exclusion limits on the parameters of the different models under consideration. Uncertainties in the signal and background predictions, and the luminosity are considered, and correlations between experimental systematic uncertainties in signal and background predictions are taken into account. The contamination of the control regions by signal events is negligible.

Table 7: Observed and expected 95% CL upper limits on the number of signal events, S^{95}_{obs} and S^{95}_{exp}, and on the visible cross section, defined as the product of cross section, acceptance and efficiency, $\langle\sigma\rangle^{95}_{obs}$, for the IM0–IM12 selections.

Selection	$\langle\sigma\rangle^{95}_{obs}$ [fb]	S^{95}_{obs}	S^{95}_{exp}
$p_{\mathrm{T}}^{\mathrm{recoil}} > 200$ GeV	861	119653	86000^{+27000}_{-24000}
$p_{\mathrm{T}}^{\mathrm{recoil}} > 250$ GeV	350	48636	35600^{+12700}_{-10000}
$p_{\mathrm{T}}^{\mathrm{recoil}} > 300$ GeV	156	21624	15500^{+6000}_{-4300}
$p_{\mathrm{T}}^{\mathrm{recoil}} > 350$ GeV	87	12066	8200^{+3100}_{-2300}
$p_{\mathrm{T}}^{\mathrm{recoil}} > 400$ GeV	52	7285	4700^{+1800}_{-1300}
$p_{\mathrm{T}}^{\mathrm{recoil}} > 500$ GeV	21	2903	1910^{+720}_{-530}
$p_{\mathrm{T}}^{\mathrm{recoil}} > 600$ GeV	10	1421	930^{+350}_{-260}
$p_{\mathrm{T}}^{\mathrm{recoil}} > 700$ GeV	4.2	578	480^{+180}_{-130}
$p_{\mathrm{T}}^{\mathrm{recoil}} > 800$ GeV	2.1	296	267^{+100}_{-75}
$p_{\mathrm{T}}^{\mathrm{recoil}} > 900$ GeV	1.2	165	161^{+62}_{-45}
$p_{\mathrm{T}}^{\mathrm{recoil}} > 1000$ GeV	1.3	189	113^{+43}_{-31}
$p_{\mathrm{T}}^{\mathrm{recoil}} > 1100$ GeV	0.5	73	71^{+27}_{-20}
$p_{\mathrm{T}}^{\mathrm{recoil}} > 1200$ GeV	0.3	39	47^{+19}_{-13}

8.2.1 Weakly interacting massive particles

As discussed in Section 1, simplified models are considered with the exchange of an axial-vector or a pseudoscalar mediator in the s-channel. In the case of the exchange of an axial-vector mediator, and for WIMP-pair production with $m_{Z_A} > 2m_\chi$, typical $A \times \epsilon$ values for the signal models with a 2 TeV mediator range from 13% to less than 1% for EM0 and EM12 selections, respectively, where the values refer to an initial simulated sample generated with a minimum transverse momentum of 150 GeV. Similarly, values for $A \times \epsilon$ in the range between 13% and less than 1% are computed for the pseudoscalar mediator model with $m_{Z_P} = 350$ GeV and $m_\chi = 1$ GeV.

Figure 5(a) shows the observed and expected 95% CL exclusion contours in the m_{Z_A}–m_χ parameter plane for a simplified model with an axial-vector mediator, Dirac WIMPs, and couplings $g_q = 1/4$ and $g_\chi = 1$. In the region $m_{Z_A} > 2 \times m_\chi$, mediator masses up to 2.1 TeV are excluded for $m_\chi = 1$ GeV, extending significantly previous bounds. The masses corresponding to the relic density [117] as determined by the Planck and WMAP satellites [15, 16], within the WIMP dark-matter model and in the absence of any interaction other than the one considered, are indicated in the Figure as a line that crosses the excluded region at $m_{Z_A} \sim 1500$ GeV and $m_\chi \sim 585$ GeV. The difference between expected and observed limits reflects the already mentioned slight excess of events observed in the tail of the measured $p_{\mathrm{T}}^{\mathrm{recoil}}$ distribution.

Similarly, Figure 5(b) presents observed and expected 95% CL exclusion contours in the m_{Z_P}–m_χ parameter plane for a simplified model with a pseudoscalar mediator, Dirac WIMPs, and couplings $g_q = 1$ and $g_\chi = 1$. For the first time, the monojet final state in the ATLAS experiment has sensitivity to exclude a part of

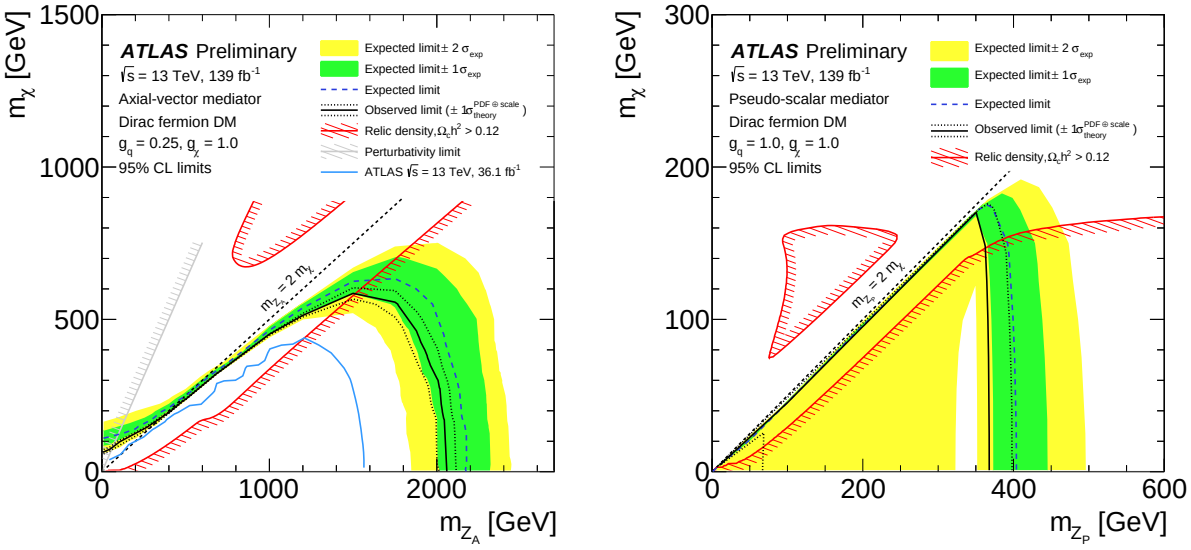

(a) (b)

Figure 5: (a) 95% CL exclusion contours in the m_{Z_A}–m_χ parameter plane for the axial-vector mediator model. (b) 95% CL exclusion contours in the m_{Z_P}–m_χ parameter plane for the pseudoscalar mediator model. The solid (dashed) curves show the observed (expected) limits, while the bands indicate the $\pm 1\sigma$ theory uncertainties in the observed limit and the $\pm 1\sigma$ and $\pm 2\sigma$ ranges of the expected limit in the absence of a signal. The red curves correspond to the set of points for which the expected relic density is consistent with the WMAP measurements (i.e. $\Omega h^2 = 0.12$), as computed with MadDM [118]. The area on the hashed side of the red contour (e.g. to the right of the red contour in the region $m_{Z_A} > 2m_\chi$) corresponds to predicted values of the relic density abundance inconsistent with the WMAP measurements. The region excluded due to perturbativity, defined by $m_\chi > \sqrt{\pi/2}\, m_{Z_A}$, is indicated by the grey hatched area. The dotted lines indicate the kinematic limit for on-shell production $m_{Z_{A,P}} = 2 \times m_\chi$. In the case of the pseudoscalar mediator model, the shape of the 2σ band at $m_{Z_P} \sim 350$ GeV is related to the rapid increase of the signal cross section at the threshold at which the mediator mass equals twice the mass of the top quark. In the case of the axial-vector mediator model, the results are compared to previous results from the ATLAS Collaboration at $\sqrt{s} = 13$ TeV [1] using 36.1 fb^{-1}.

the parameter space in such model. Mediator masses below 367 GeV are excluded for very light WIMP candidates.

In the case of the axial-vector mediator model, the results are translated into 90% CL exclusion limits on the spin-dependent WIMP–nucleon scattering cross section σ_{SD} as a function of the WIMP mass, following the prescriptions from Refs. [19, 117]. Figure 6 shows exclusion limits for WIMP–proton and WIMP–neutron scattering cross sections as a function of the WIMP mass, compared to the results from the PICO [119] experiment, and the LUX [120] and XENON1T [121] experiments, respectively. Stringent limits on the scattering cross section of the order of 9.8×10^{-44} cm^2 for WIMP masses of about 100 GeV, and 3.7×10^{-44} cm^2 for WIMP masses below 10 GeV are inferred from this analysis, which complement the results from direct-detection experiments.

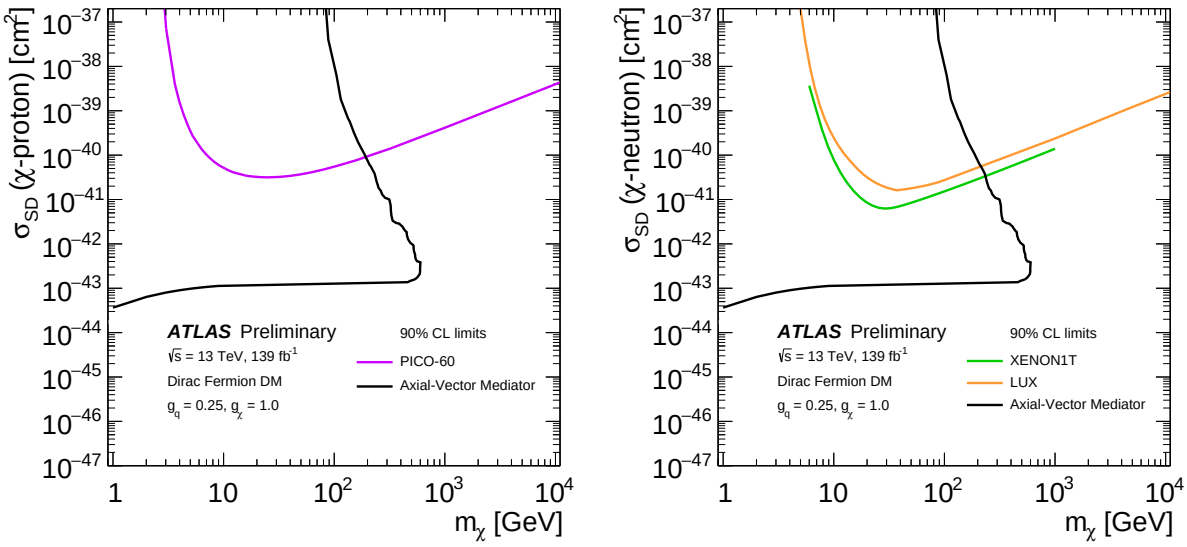

(a) (b)

Figure 6: A comparison of the inferred limits (black line) to the constraints from direct detection experiments on the spin-dependent (a) WIMP–proton scattering cross section and (b) WIMP–neutron scattering cross section as a function of the WIMP mass, in the context of the simplified model with axial-vector couplings. Unlike in the m_{Z_A}–m_χ parameter plane, the limits are shown at 90% CL. The results from this analysis, excluding the region to the left of the contour, are compared with limits from the PICO [119] (purple line), LUX [120] (orange line), and XENON1T [121] (green line) experiments. The comparison is model-dependent and solely valid in the context of this model, assuming minimal mediator width and the coupling values $g_q = 1/4$ and $g_\chi = 1$.

8.2.2 Squark-pair production

As in previous publications, different models of squark-pair production are considered: stop-pair production with $\tilde{t}_1 \rightarrow c + \tilde{\chi}_1^0$, stop-pair production with $\tilde{t}_1 \rightarrow b + f f' + \tilde{\chi}_1^0$, sbottom-pair production with $\tilde{b}_1 \rightarrow b + \tilde{\chi}_1^0$, and squark-pair production with $\tilde{q} \rightarrow q + \tilde{\chi}_1^0$ ($q = u, d, c, s$). In each case separately, the results are translated into exclusion limits as a function of the squark mass for different neutralino masses. The region with stop–neutralino or sbottom-neutralino mass differences below 5 GeV is not considered in the exclusion since in this regime the squarks could become long-lived. In such a compressed scenario, and for stop sbottom masses of about 600 GeV, the typical value of $A \times \epsilon$ of the selection criteria varies between 11% for EM0 and less than 1% for EM12, as computed using a sample with a minimum missing transverse momentum of 150 GeV. Comparable values for $A \times \epsilon$ are obtained in the rest of the squark-neutralino mass plane.

Figure 7(a) presents the results in the case of the $\tilde{t}_1 \rightarrow c + \tilde{\chi}_1^0$ decays. In the compressed scenario with stop and neutralino nearly degenerate in mass, masses up to 550 GeV are excluded. This is significantly less than the expected exclusion reach of about 600 GeV. As already discussed, the difference between expected and observed exclusions is the result of the slight excess of events in data observed in the $p_{\mathrm{T}}^{\mathrm{recoil}}$ distribution. Similarly, Figure 7(b) shows the observed and expected 95% CL exclusion limits as a function of the stop and neutralino masses for the $\tilde{t}_1 \rightarrow b + f f' + \tilde{\chi}_1^0$ (BR=100%) decay channel. For $m_{\tilde{t}_1} - m_{\tilde{\chi}_1^0} \sim m_b$, stop masses up to 550 GeV are also excluded. Figure 8(a) presents the observed and expected 95% CL exclusion limits as a function of the sbottom and neutralino masses for the $\tilde{b}_1 \rightarrow b + \tilde{\chi}_1^0$ (BR=100%) decay channel.

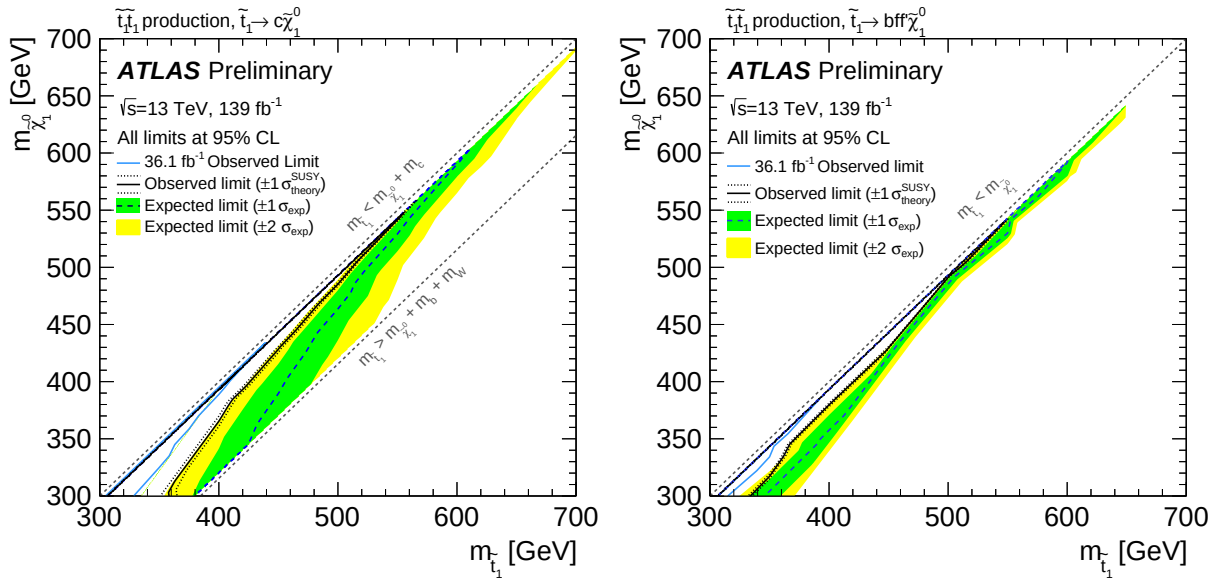

(a) (b)

Figure 7: Excluded regions at the 95% CL in the $(\tilde{t}_1, \tilde{\chi}_1^0)$ mass plane for (a) the decay channel $\tilde{t}_1 \to c + \tilde{\chi}_1^0$ (BR=100%) and (b) the decay channel $\tilde{t}_1 \to b + ff' + \tilde{\chi}_1^0$ (BR=100%). The dotted lines around the observed limits indicate the range of observed limits corresponding to $\pm 1\sigma$ variations of the NNLO + NNLL SUSY cross-section predictions. The bands around the expected limits indicate the expected $\pm 1\sigma$ and $\pm 2\sigma$ ranges of limits in the absence of a signal. The results from this analysis are compared to previous results from the ATLAS Collaboration at $\sqrt{s} = 13$ TeV [1] using 36.1 fb^{-1}.

In the scenario with $m_{\tilde{b}_1} - m_{\tilde{\chi}_1^0} \sim m_b$, this analysis extends the 95% CL exclusion limits up to a sbottom mass of 550 GeV. Finally, Figure 8(b) presents the observed and expected 95% CL exclusion limits as a function of the squark mass and the squark–neutralino mass difference for $\tilde{q} \to q + \tilde{\chi}_1^0$ ($q = u, d, c, s$). In the compressed scenario, squark masses below 900 GeV are excluded at 95% CL. Altogether, these results improve significantly previous exclusion limits based on 36.1 fb^{-1} of total integrated luminosity [1]. In the very compressed scenario, the observed limits on the squark masses are extended by more than 100 GeV.

8.2.3 Dark Energy inspired model

Exclusion limits are computed for the Horndeski dark energy model (see Section 1) with $m_\varphi = 0.1$ GeV, and considering only the terms relevant for the monojet final state, following the work described in Refs. [6, 122]. The sensitivity remains independent of the m_φ value considered for light particles up to masses of the order of 1 GeV. The typical value of $A \times \epsilon$ of the selection criteria varies between 9% for EM0 and less than 1% for EM12. Figure 9 shows the observed and expected contours at 95% CL on the $\sigma - M_2$ plane. Values for M_2 below 1558 GeV are excluded, which represents a significant improvement over the limits previously obtained [122]. The validity of the effective implementation of the model at the LHC energies was studied previously [6] by truncating the signal contributions with $\sqrt{\hat{s}} < g_* M_2$, where $\sqrt{\hat{s}}$ is the centre-of-mass energy of the hard interaction, leading to a negligible effect in the obtained exclusion limits.

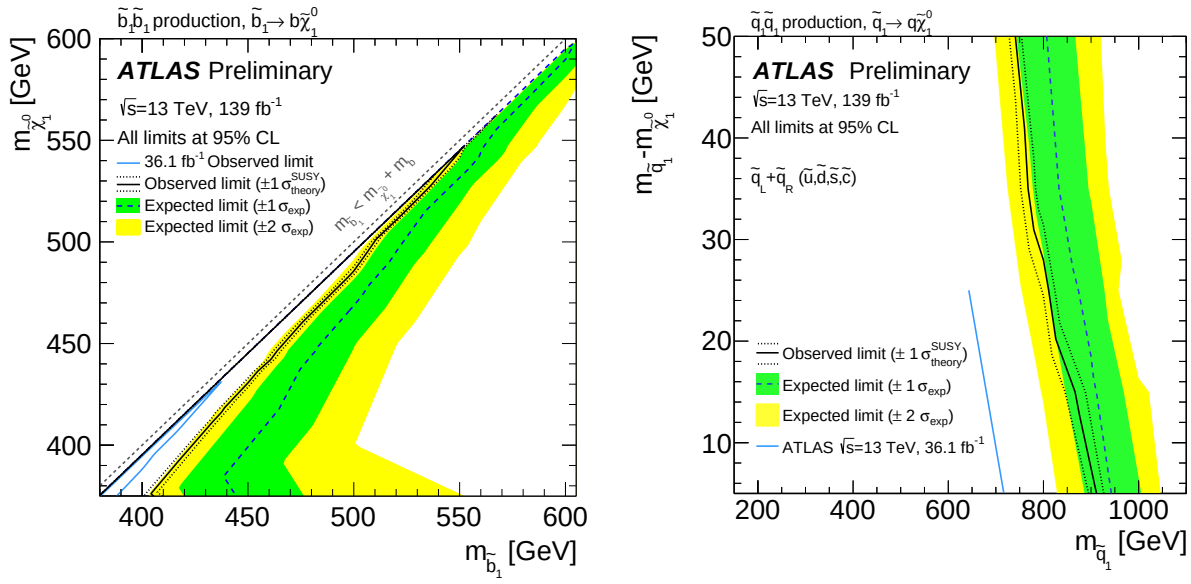

(a) (b)

Figure 8: (a) Exclusion plane at 95% CL as a function of sbottom and neutralino masses for the decay channel $\tilde{b}_1 \to b + \tilde{\chi}_1^0$ (BR=100%). (b) Exclusion region at 95% CL as a function of squark mass and the squark–neutralino mass difference for $\tilde{q} \to q + \tilde{\chi}_1^0$ and $\tilde{q_L} + \tilde{q_R}$ with ($\tilde{u}, \tilde{d}, \tilde{c}, \tilde{s}$). The dotted lines around the observed limit indicate the range of observed limits corresponding to $\pm 1\sigma$ variations of the NNLO + NNLL SUSY cross-section predictions. The bands around the expected limit indicates the expected $\pm 1\sigma$ and $\pm 2\sigma$ ranges of limits in the absence of a signal. The results from this analysis are compared to previous results from the ATLAS Collaboration at $\sqrt{s}$ = 13 TeV [1] using 36.1 fb^{-1}.

8.2.4 Large extra spatial dimensions

The results are translated into limits on the parameters of the ADD model. As in previous analyses, only the signal regions with $p_{\mathrm{T}}^{\mathrm{recoil}} > 400$ GeV are employed, with sufficient sensitivity to ADD signal. The typical value of $A \times \epsilon$ of the selection criteria, as computed from a simulated sample with missing transverse momentum above 150 GeV, is of the order of 6% for EM4 and is less than 1% for EM12. Figure 10 and Table 8 present the results. Values of M_D below 11.7 TeV at $n = 2$ and below 5.9 TeV at $n = 6$ are excluded at 95% CL, which improve on the exclusion limits from previous results using 36.1 fb^{-1} of 13 TeV data [1]. As already noted in Ref. [1], the analysis partially probes the phase-space region with $\hat{s} > M_D^2$. The suppression of this kinematic region in computing the 95% CL lower limits on M_D translates into a negligible effect on the results.

8.2.5 Axion-like particles

Results are expressed in terms of 95% CL limits on the parameters of the ALP model. As in the case of the ADD model, the kinematic region with $p_{\mathrm{T}}^{\mathrm{recoil}} > 400$ GeV provides the best sensitivity. Figure 11 shows 95% exclusion contours in the the $c_{\tilde{G}} - f_a$ plane, for an axion mass of 1 MeV. The exclusion does not depend significantly on the axion mass for masses up to at least 1 GeV. The limits on $c_{\tilde{G}}$ increase linearly with f_a. For $f_a = 1$ TeV, couplings $c_{\tilde{G}}$ above 0.008 are excluded. Expressed in terms of the $c_{\tilde{G}}/f_a$ ratio,

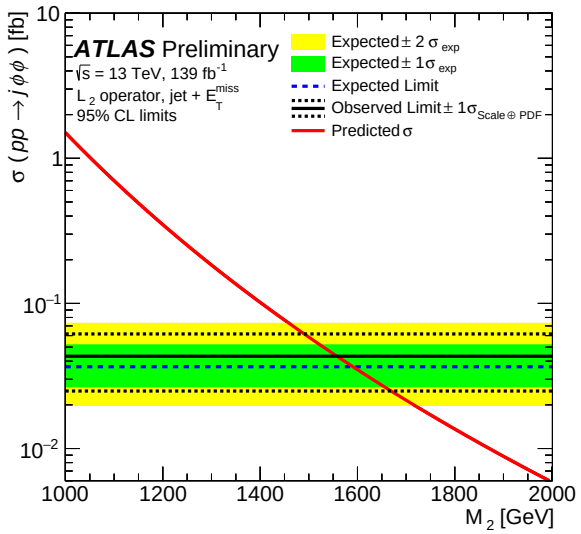

Figure 9: Observed (solid line) and expected (dashed line) exclusions at 95% CL on the Horndeski dark energy model for $m_\phi = 0.1$ GeV and $c_{i\neq 2} = 0$, $c_2 = 1$ [122], expressed in term of visible cross section as a function of of the suppression scale M_2. The results are compared to the theoretical predictions. The dotted lines around the observed limits indicate the range of observed limits corresponding to $\pm 1\sigma$ variations of the cross-section predictions.

values above $8 \times 10^{-6}\,\text{GeV}^{-1}$ are excluded at 95% CL. As in the case of the dark energy and ADD models, the validity of the effective field implementation of the model is challenged for $\hat{s} > f_a^2$. For values of f_a below 2 TeV, the signal yields are reduced significantly when applying a suppressing weighting factor $f_a^4/\hat{s}^2$ for events with $\hat{s} > f_a^2$. The effect is reduced to about 5% for $f_a = 2$ TeV and it is negligible for f_a above 3 TeV.

Table 8: The 95% CL observed and expected lower limits on the fundamental Planck scale in $4 + n$ dimensions, M_D, as a function of the number of extra dimensions n, considering nominal LO signal cross sections. The impact of the $\pm 1\sigma$ theoretical uncertainty on the observed limits and the expected $\pm 1\sigma$ range of limits in the absence of a signal are also given.

	ADD Model Limits on M_D (95% CL)	
	Expected [TeV]	Observed [TeV]
n = 2	$11.7^{+1.0}_{-1.0}$	$11.3^{+1.0}_{-1.3}$
n = 3	$8.7^{+0.6}_{-0.6}$	$8.5^{+0.6}_{-0.8}$
n = 4	$7.2^{+0.4}_{-0.4}$	$7.1^{+0.4}_{-0.6}$
n = 5	$6.4^{+0.3}_{-0.3}$	$6.4^{+0.3}_{-0.5}$
n = 6	$5.9^{+0.3}_{-0.3}$	$5.9^{+0.3}_{-0.4}$

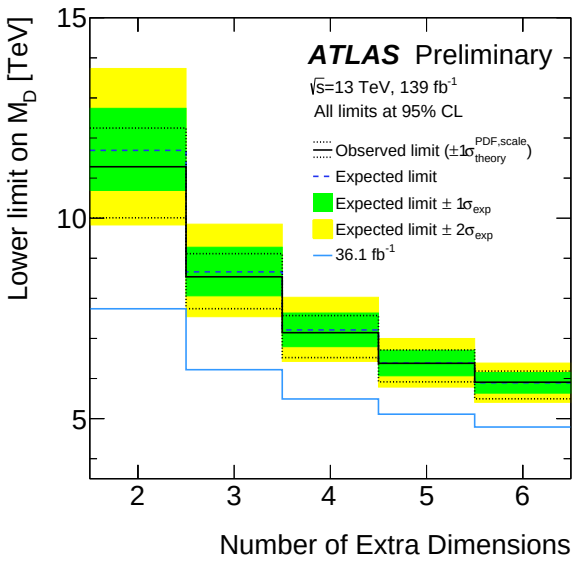

Figure 10: Observed and expected 95% CL lower limits on the fundamental Planck scale in $4 + n$ dimensions, M_D, as a function of the number of extra dimensions. The bands indicate the $\pm 1\sigma$ theory uncertainties in the observed limit and the $\pm 1\sigma$ and $\pm 2\sigma$ ranges of the expected limit in the absence of a signal. The results from this analysis are compared to previous results from the ATLAS Collaboration using 36.1fb^{-1} of $\sqrt{s} = 13$ TeV data [1].

8.2.6 Invisibly-decaying Higgs boson

The results are interpreted in terms of 95% CL upper limits on the branching ratio for an invisibly decaying Higgs boson. The signal yields are dominated by gluon-gluon initiated processes (about 54%), followed by the contributions from VBF (34%) and VH (12%) processes. The low $E_{\mathrm{T}}^{\mathrm{miss}}$ region plays an important role in enhancing the sensitivity of the data to the Higgs signal and the full $E_{\mathrm{T}}^{\mathrm{miss}}$ spectrum is employed in computing the limits. The observed agreement between data and the SM background predictions in the measured $E_{\mathrm{T}}^{\mathrm{miss}}$ distribution leads to a 95% CL observed (expected) exclusion limit on the invisible branching ratio of the Higgs boson of 0.63 (0.57).

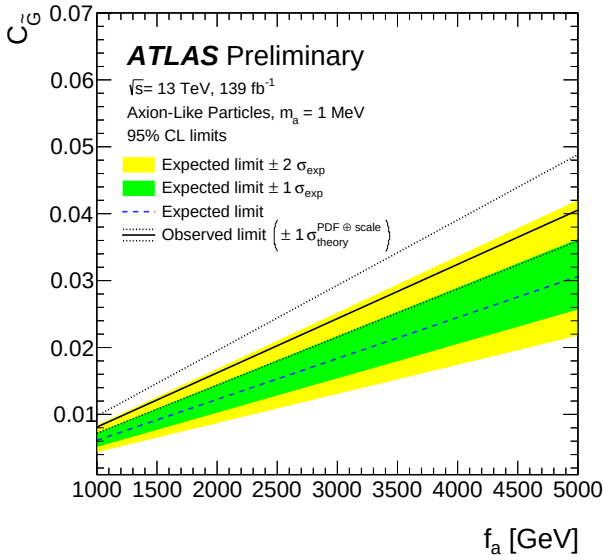

Figure 11: Observed and expected 95% CL lower limits on the coupling $c_{\tilde{G}}$ as a function of the effective scale f_a for ALP mass of 1 MeV. The bands indicate the $\pm 1\sigma$ theory uncertainties in the observed limit and the $\pm 1\sigma$ and $\pm 2\sigma$ ranges of the expected limit in the absence of a signal. The 95% CL limits are computed with no suppression of the events with $\hat{s} > f_a^2$.

9 Conclusions

Results are reported from a search for new phenomena in events with an energetic jet and large missing transverse momentum in proton–proton collisions at $\sqrt{s} = 13$ TeV at the LHC, based on data corresponding to an integrated luminosity of 139 fb^{-1} collected by the ATLAS detector in the 2015 – 2018 period. The measurements are in agreement with the SM predictions. The results are translated into model-independent 95% CL upper limits on the visible cross section for new phenomena in the range between 861 – 0.3 fb with increasing missing transverse momentum. Improved bounds on the parameters for a variety of models for new phenomena have been derived. In the case of simplified models for WIMP-pair production in the s-channel, with Dirac fermions as dark-matter candidates, an axial-vector mediator with masses below 2.1 TeVis excluded at 95% CL for very light WIMPs and coupling values $g_q = 1/4$ and $g_\chi = 1$. For the first time, the ATLAS monojet analysis reaches sensitivity for excluding pseudoscalar mediators with masses below 367 GeV, for very light WIMPs and coupling values $g_q = 1$ and $g_\chi = 1$.

Similarly, the results are interpreted in terms of a search for squark-pair production in a compressed-mass supersymmetric scenario. In the case of stop- and sbottom-pair production with $\tilde{t}_1 \rightarrow c + \tilde{\chi}_1^0$ or $\tilde{t}_1 \rightarrow b + f f^{'} + \tilde{\chi}_1^0$ and $\tilde{b}_1 \rightarrow b + \tilde{\chi}_1^0$, respectively, squark masses below about 550 GeV are excluded at 95% CL, thus increasing by almost 100 GeV previous exclusions. In the case of squark-pair production with $\tilde{q} \rightarrow q + \tilde{\chi}_1^0$ ($q = u, d, c, s$), squark masses below 900 GeV are excluded.

The results are expressed in terms of 95% CL limits to the suppression scale M_2 for the Horndeski dark energy model with $m_\phi = 0.1$ GeV and $c_{i\neq 2} = 0$, $c_2 = 1$. Suppression scales M_2 above 1.5 TeV are excluded. In the case of the ADD model with large extra spatial dimensions, lower 95% CL limits on the fundamental Planck scale M_D in $4 + n$ dimensions vary in the range between 11.7 TeV and 5.9 TeV for $n = 2$ and n=6,

respectively. In models with axion-like particles with coupling to gluons, couplings-to-effective scale ratios $c_{\tilde{G}}/f_a$ above 8×10^{-6} GeV $^{-1}$ are excluded at 95% CL for axion masses up to 1 GeV. Finally, limits are obtained for the branching ratio of an invisibly decaying Higgs boson. Branching fractions above 0.63 are excluded at 95% CL.

Appendix

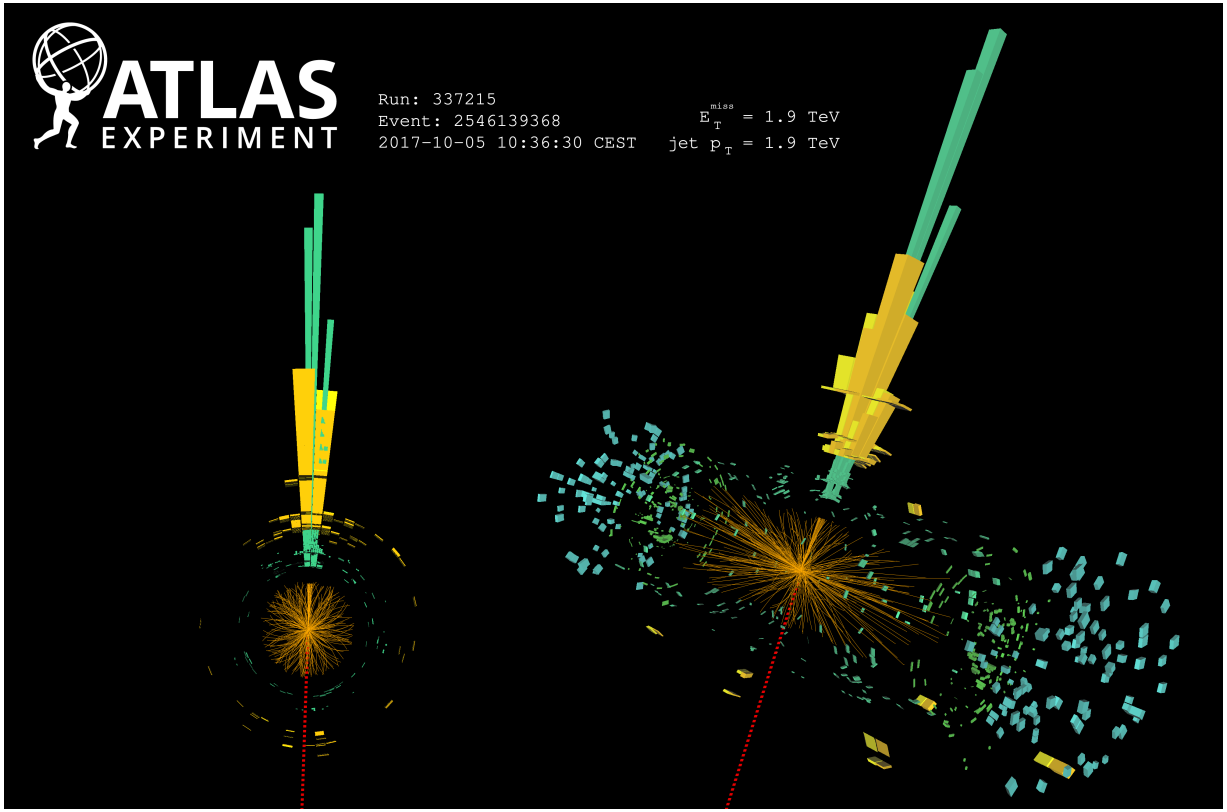

Figure 12: A monojet event with jet p_{T} = 1924 GeVand $p_{\mathrm{T}}^{\mathrm{recoil}}$ = 1913 GeV collected in the 2017 ATLAS dataset (Event = 2546139368, Run = 337215). No additional jets with p_{T} above 30 GeV are found. Green and yellow bars correspond to the energy depositions in the electromagnetic and hadronic calorimeters, respectively. The missing transverse momentum is shown as the red dashed line on the opposite side of the detector.

References

[1] ATLAS Collaboration, *Search for dark matter and other new phenomena in events with an energetic jet and large missing transverse momentum using the ATLAS detector*, JHEP **01** (2018) 126, arXiv: 1711.03301 [hep-ex].

[2] ATLAS Collaboration, *Search for new phenomena in final states with an energetic jet and large missing transverse momentum in pp collisions at* $\sqrt{s}$ = 13 *TeV using the ATLAS detector*, Phys. Rev. D **94** (2016) 032005, arXiv: 1604.07773 [hep-ex].

[3] CMS Collaboration, *Search for dark matter produced with an energetic jet or a hadronically decaying W or Z boson at* $\sqrt{s}$ = 13 *TeV*, JHEP **07** (2017) 014, arXiv: 1703.01651 [hep-ex].

[4] ATLAS Collaboration, *Measurement of detector-corrected observables sensitive to the anomalous production of events with jets and large missing transverse momentum in pp collisions at* $\sqrt{\mathbf{s}}$ = **13** *TeV using the ATLAS detector*, Eur. Phys. J. C **77** (2017) 765, arXiv: 1707.03263 [hep-ex].

[5] CMS Collaboration, *Search for dark matter, extra dimensions, and unparticles in monojet events in proton–proton collisions at* $\sqrt{s}$ = 8 *TeV*, Eur. Phys. J. C **75** (2015) 235, arXiv: 1408.3583 [hep-ex].

[6] ATLAS Collaboration, *Constraints on mediator-based dark matter and scalar dark energy models using* $\sqrt{s}$ = 13 *TeV pp collision data collected by the ATLAS detector*, JHEP **05** (2019) 142, arXiv: 1903.01400 [hep-ex].

[7] K. Mimasu and V. Sanz, *ALPs at Colliders*, JHEP **06** (2015) 173, arXiv: 1409.4792 [hep-ph].

[8] ATLAS Collaboration, *Search for new phenomena in final states with an energetic jet and large missing transverse momentum in pp collisions at* $\sqrt{s}$ *=8 TeV with the ATLAS detector*, Eur. Phys. J. **C75** (2015) 299, [Erratum: Eur. Phys. J.C75,no.9,408(2015)], arXiv: 1502.01518 [hep-ex].

[9] CMS Collaboration, *Searches for invisible decays of the Higgs boson in pp collisions at* $\sqrt{s}$ *= 7, 8, and 13 TeV*, JHEP **02** (2017) 135, arXiv: 1610.09218 [hep-ex].

[10] V. Trimble, *Existence and Nature of Dark Matter in the Universe*, Ann. Rev. Astron. Astrophys. **25** (1987) 425.

[11] G. Bertone, D. Hooper and J. Silk, *Particle dark matter: Evidence, candidates and constraints*, Phys. Rept. **405** (2005) 279, arXiv: hep-ph/0404175.

[12] J. L. Feng, *Dark Matter Candidates from Particle Physics and Methods of Detection*, Ann. Rev. Astron. Astrophys. **48** (2010) 495, arXiv: 1003.0904 [astro-ph.CO].

[13] G. Steigman and M. S. Turner, *Cosmological Constraints on the Properties of Weakly Interacting Massive Particles*, Nucl. Phys. B **253** (1985) 375.

[14] E. W. Kolb and M. S. Turner, *The Early Universe*, Front. Phys. **69** (1990) 1.

[15] R. Adam, et al., Planck Collaboration, *Planck 2018 results. VI. Cosmological parameters*, (2018), arXiv: 1807.06209 [astro-ph.CO].

[16] G. Hinshaw et al., *Nine-year Wilkinson Microwave Anisotropy Probe (WMAP) Observations: Cosmological Parameter Results*, ApJS **208** (2013) 19, arXiv: 1212.5226 [astro-ph.CO].

[17] J. Abdallah et al., *Simplified Models for Dark Matter Searches at the LHC*, Phys. Dark Univ. **9-10** (2015) 8, arXiv: 1506.03116 [hep-ph].

[18] D. Abercrombie et al., *Dark Matter benchmark models for early LHC Run-2 Searches: Report of the ATLAS/CMS Dark Matter Forum*, Physics of the Dark Universe **27** (2020) 100371, ISSN: 2212-6864, URL: http://www.sciencedirect.com/science/article/pii/S2212686419301712.

[19] O. Buchmueller, M. J. Dolan, S. A. Malik and C. McCabe, *Characterising dark matter searches at colliders and direct detection experiments: Vector mediators*, JHEP **01** (2015) 037, arXiv: 1407.8257 [hep-ph].

[20] H. Miyazawa, *Baryon Number Changing Currents*, Prog. Theor. Phys. **36** (1966) 1266.

[21] P. Ramond, *Dual Theory for Free Fermions*, Phys. Rev. D **3** (1971) 2415.

[22] Y. A. Golfand and E. P. Likhtman, *Extension of the Algebra of Poincare Group Generators and Violation of p Invariance*, JETP Lett. **13** (1971) 323.

[23] A. Neveu and J. H. Schwarz, *Factorizable dual model of pions*, Nucl. Phys. B **31** (1971) 86.

[24] A. Neveu and J. H. Schwarz, *Quark Model of Dual Pions*, Phys. Rev. D **4** (1971) 1109.

[25] J. Gervais and B. Sakita, *Field theory interpretation of supergauges in dual models*, Nucl. Phys. B **34** (1971) 632.

[26] D. V. Volkov and V. P. Akulov, *Is the Neutrino a Goldstone Particle?*, Phys. Lett. B **46** (1973) 109.

[27] J. Wess and B. Zumino, *A Lagrangian Model Invariant Under Supergauge Transformations*, Phys. Lett. B **49** (1974) 52.

[28] J. Wess and B. Zumino, *Supergauge Transformations in Four-Dimensions*, Nucl. Phys. B **70** (1974) 39.

[29] P. Fayet, *Supersymmetry and Weak, Electromagnetic and Strong Interactions*, Phys. Lett. B **64** (1976) 159.

[30] P. Fayet, *Spontaneously Broken Supersymmetric Theories of Weak, Electromagnetic and Strong Interactions*, Phys. Lett. B **69** (1977) 489.

[31] G. R. Farrar and P. Fayet, *Phenomenology of the Production, Decay, and Detection of New Hadronic States Associated with Supersymmetry*, Phys. Lett. B **76** (1978) 575.

[32] P. Fayet, *Relations Between the Masses of the Superpartners of Leptons and Quarks, the Goldstino Couplings and the Neutral Currents*, Phys. Lett. B **84** (1979) 416.

[33] S. Dimopoulos and H. Georgi, *Softly Broken Supersymmetry and SU(5)*, Nucl. Phys. B **193** (1981) 150.

[34] A. G. Riess et al., *Observational evidence from supernovae for an accelerating universe and a cosmological constant*, Astron. J. **116** (1998) 1009, arXiv: astro-ph/9805201 [astro-ph].

[35] S. Perlmutter et al., *Measurements of Ω and Λ from 42 high redshift supernovae*, Astrophys. J. **517** (1999) 565, arXiv: astro-ph/9812133 [astro-ph].

[36] P. Brax, C. Burrage, C. Englert and M. Spannowsky, *LHC Signatures Of Scalar Dark Energy*, Phys. Rev. **D94** (2016) 084054, arXiv: 1604.04299 [hep-ph].

[37] G. W. Horndeski, *Second-order scalar-tensor field equations in a four-dimensional space*, International Journal of Theoretical Physics **10** (1974) 363, URL: https://doi.org/10.1007/BF01807638.

[38] H. Georgi, *Effective Field Theory*, Annual Review of Nuclear and Particle Science **43** (1993) 209, URL: https://doi.org/10.1146/annurev.ns.43.120193.001233.

[39] N. Arkani-Hamed, S. Dimopoulos and G. Dvali, *The hierarchy problem and new dimensions at a millimeter*, Phys. Lett. B **429** (1998) 263, arXiv: hep-ph/9803315.

[40] R. D. Peccei and H. R. Quinn, *CP Conservation in the Presence of Instantons*, Phys. Rev. Lett. **38** (1977) 1440.

[41] I. Brivio et al., *ALPs Effective Field Theory and Collider Signatures*, Eur. Phys. J. **C77** (2017) 572, arXiv: 1701.05379 [hep-ph].

[42] ATLAS Collaboration, *Combination of searches for invisible Higgs boson decays with the ATLAS experiment*, Phys. Rev. Lett. **122** (2019) 231801, arXiv: 1904.05105 [hep-ex].

[43] CMS Collaboration, *Search for invisible decays of a Higgs boson produced through vector boson fusion in proton-proton collisions at* $\sqrt{s}$ *= 13 TeV*, Phys. Lett. B **793** (2019) 520, arXiv: 1809.05937 [hep-ex].

[44] ATLAS Collaboration, *The ATLAS Experiment at the CERN Large Hadron Collider*, JINST **3** (2008) S08003.

[45] ATLAS Collaboration, *ATLAS Insertable B-Layer Technical Design Report*, ATLAS-TDR-19, 2010, URL: https://cds.cern.ch/record/1291633.

[46] B. Abbott et al., *Production and integration of the ATLAS Insertable B-Layer*, JINST **13** (2018) T05008, arXiv: 1803.00844 [physics.ins-det].

[47] ATLAS Collaboration, *Performance of the ATLAS trigger system in 2015*, Eur. Phys. J. C **77** (2017) 317, arXiv: 1611.09661 [hep-ex].

[48] ATLAS Collaboration, *The ATLAS Simulation Infrastructure*, Eur. Phys. J. C **70** (2010) 823, arXiv: 1005.4568 [physics.ins-det].

[49] S. Agostinelli et al., *GEANT4 – a simulation toolkit*, Nucl. Instrum. Meth. A **506** (2003) 250.

[50] D. J. Lange, *The EvtGen particle decay simulation package*, Nucl. Instrum. Meth. A **462** (2001) 152.

[51] T. Sjöstrand, S. Mrenna and P. Z. Skands, *PYTHIA 6.4 physics and manual*, JHEP **05** (2006) 026, arXiv: hep-ph/0603175.

[52] ATLAS Collaboration, *The Pythia 8 A3 tune description of ATLAS minimum bias and inelastic measurements incorporating the Donnachie–Landshoff diffractive model*, ATL-PHYS-PUB-2016-017, 2016, URL: https://cds.cern.ch/record/2206965.

[53] R. D. Ball et al., *Parton distributions for the LHC run II*, JHEP **04** (2015) 040, arXiv: 1410.8849 [hep-ph].

[54] ATLAS Collaboration, *ATLAS Pythia 8 tunes to 7 TeV data*, ATL-PHYS-PUB-2014-021, 2014, URL: https://cds.cern.ch/record/1966419.

[55] J. Alwall et al., *The automated computation of tree-level and next-to-leading order differential cross sections, and their matching to parton shower simulations*, JHEP **07** (2014) 079, arXiv: 1405.0301 [hep-ph].

[56] L. Lönnblad and S. Prestel, *Matching tree-level matrix elements with interleaved showers*, Journal of High Energy Physics **03** (2012) 019, arXiv: 1109.4829 [hep-ph].

[57] W. Beenakker, M. Kramer, T. Plehn, M. Spira and P. M. Zerwas, *Stop production at hadron colliders*, Nucl. Phys. B **515** (1998) 3, arXiv: hep-ph/9710451.

[58] W. Beenakker et al., *Supersymmetric top and bottom squark production at hadron colliders*, JHEP **08** (2010) 098, arXiv: 1006.4771 [hep-ph].

[59] W. Beenakker, C. Borschensky, M. Krämer, A. Kulesza and E. Laenen, *NNLL-fast: predictions for coloured supersymmetric particle production at the LHC with threshold and Coulomb resummation*, JHEP **12** (2016) 133, arXiv: 1607.07741 [hep-ph].

[60] W. Beenakker et al., *NNLL resummation for stop pair-production at the LHC*, JHEP **05** (2016) 153, arXiv: 1601.02954 [hep-ph].

[61] C. Borschensky et al., *Squark and gluino production cross sections in pp collisions at $\sqrt{s}$ = 13, 14, 33 and 100 TeV*, Eur. Phys. J. C **74** (2014) 3174, arXiv: 1407.5066 [hep-ph].

[62] S. Alioli, P. Nason, C. Oleari and E. Re, *A general framework for implementing NLO calculations in shower Monte Carlo programs: the POWHEG BOX*, JHEP **06** (2010) 043, arXiv: 1002.2581 [hep-ph].

[63] S. Frixione, P. Nason and C. Oleari, *Matching NLO QCD computations with parton shower simulations: the POWHEG method*, JHEP **11** (2007) 070, arXiv: 0709.2092 [hep-ph].

[64] P. Nason, *A new method for combining NLO QCD with shower Monte Carlo algorithms*, JHEP **11** (2004) 040, arXiv: hep-ph/0409146.

[65] U. Haisch, F. Kahlhöfer and E. Re, *QCD effects in mono-jet searches for dark matter*, JHEP **12** (2013) 007, arXiv: 1310.4491 [hep-ph].

[66] U. Haisch and E. Re, *Simplified dark matter top-quark interactions at the LHC*, JHEP **06** (2015) 078, arXiv: 1503.00691 [hep-ph].

[67] ATLAS Collaboration, *ATLAS Run 1 Pythia8 tunes*, ATL-PHYS-PUB-2014-021, 2014, URL: https://cds.cern.ch/record/1966419.

[68] S. Frixione, P. Nason and G. Ridolfi, *A Positive-weight next-to-leading-order Monte Carlo for heavy flavour hadroproduction*, JHEP **09** (2007) 126, arXiv: 0707.3088 [hep-ph].

[69] ATLAS Collaboration, *Measurement of the Z/γ^* boson transverse momentum distribution in pp collisions at $\sqrt{s}$ = 7 TeV with the ATLAS detector*, JHEP **09** (2014) 145, arXiv: 1406.3660 [hep-ex].

[70] LHC Higgs Cross Section Working Group, D. de Florian et al., *Handbook of LHC Higgs Cross Sections: 4. Deciphering the Nature of the Higgs Sector*, (2016), arXiv: 1610.07922 [hep-ph].

[71] T. Gleisberg et al., *Event generation with SHERPA 1.1*, JHEP **02** (2009) 007, arXiv: 0811.4622 [hep-ph].

[72] F. Cascioli, P. Maierhöfer and S. Pozzorini, *Scattering Amplitudes with Open Loops*, Phys. Rev. Lett. **108** (2012) 111601, arXiv: 1111.5206 [hep-ph].

[73] T. Gleisberg and S. Höche, *Comix, a new matrix element generator*, JHEP **12** (2008) 039, arXiv: 0808.3674 [hep-ph].

[74] S. Schumann and F. Krauss, *A parton shower algorithm based on Catani–Seymour dipole factorisation*, JHEP **03** (2008) 038, arXiv: 0709.1027 [hep-ph].

[75] S. Höche, F. Krauss, M. Schönherr and F. Siegert, *QCD matrix elements + parton showers. The NLO case*, JHEP **04** (2013) 027, arXiv: 1207.5030 [hep-ph].

[76] S. Catani, L. Cieri, G. Ferrera, D. de Florian and M. Grazzini, *Vector boson production at hadron colliders: a fully exclusive QCD calculation at NNLO*, Phys. Rev. Lett. **103** (2009) 082001, arXiv: 0903.2120 [hep-ph].

[77] S. Catani and M. Grazzini, *An NNLO subtraction formalism in hadron collisions and its application to Higgs boson production at the LHC*, Phys. Rev. Lett. **98** (2007) 222002, arXiv: hep-ph/0703012.

[78] A. D. Martin, W. J. Stirling, R. S. Thorne and G. Watt, *Parton distributions for the LHC*, Eur. Phys. J. C **63** (2009) 189, arXiv: 0901.0002 [hep-ph].

[79] J. M. Lindert et al., *Precise predictions for V+jets dark matter backgrounds*, The European Physical Journal C **77** (2017) 829, ISSN: 1434-6052, URL: https://doi.org/10.1140/epjc/s10052-017-5389-1.

[80] ATLAS Collaboration, *Measurements of the production cross section of a Z boson in association with jets in pp collisions at* $\sqrt{s}$ = 13 *TeV with the ATLAS detector*, Eur. Phys. J. C **77** (2017) 361, arXiv: 1702.05725 [hep-ex].

[81] M. Bahr et al., *Herwig++ Physics and Manual*, Eur. Phys. J. C **58** (2008) 639, arXiv: 0803.0883 [hep-ph].

[82] J. Baglio et al., *Release Note - VBFNLO 2.7.0*, (2014), arXiv: 1404.3940 [hep-ph].

[83] H.-L. Lai et al., *New parton distributions for collider physics*, Phys. Rev. D **82** (2010) 074024, arXiv: 1007.2241 [hep-ph].

[84] C. D. White, S. Frixione, E. Laenen and F. Maltoni, *Isolating Wt production at the LHC*, JHEP **11** (2009) 074, arXiv: 0908.0631 [hep-ph].

[85] J. M. Campbell, R. K. Ellis and C. Williams, *Vector boson pair production at the LHC*, JHEP **07** (2011) 018, arXiv: 1105.0020 [hep-ph].

[86] M. Cacciari, G. P. Salam and G. Soyez, *The anti-*k_t *jet clustering algorithm*, JHEP **04** (2008) 063, arXiv: 0802.1189 [hep-ph].

[87] M. Cacciari, G. P. Salam and G. Soyez, *FastJet user manual*, Eur. Phys. J. C **72** (2012) 1896, arXiv: 1111.6097 [hep-ph].

[88] ATLAS Collaboration, *Jet energy scale measurements and their systematic uncertainties in proton–proton collisions at* $\sqrt{s}$ = 13 *TeV with the ATLAS detector*, Phys. Rev. D **96** (2017) 072002, arXiv: 1703.09665 [hep-ex].

[89] ATLAS Collaboration, *Jet energy measurement with the ATLAS detector in proton–proton collisions at* $\sqrt{s}$ = 7 *TeV*, Eur. Phys. J. C **73** (2013) 2304, arXiv: 1112.6426 [hep-ex].

[90] ATLAS Collaboration, *Tagging and suppression of pileup jets with the ATLAS detector*, ATLAS-CONF-2014-018, 2014, URL: https://cds.cern.ch/record/1700870.

[91] ATLAS Collaboration, *Performance of b-jet identification in the ATLAS experiment*, JINST **11** (2016) P04008, arXiv: 1512.01094 [hep-ex].

[92] ATLAS Collaboration, *Optimisation of the ATLAS b-tagging performance for the 2016 LHC Run*, ATL-PHYS-PUB-2016-012, 2016, URL: https://cds.cern.ch/record/2160731.

[93] ATLAS Collaboration, *Electron efficiency measurements with the ATLAS detector using the 2012 LHC proton–proton collision data*, ATLAS-CONF-2014-032, 2014, URL: https://cds.cern.ch/record/1706245.

[94] ATLAS Collaboration, *Muon reconstruction performance of the ATLAS detector in proton–proton collision data at* $\sqrt{s}$ = 13 *TeV*, Eur. Phys. J. C **76** (2016) 292, arXiv: 1603.05598 [hep-ex].

[95] ATLAS Collaboration, *Identification and energy calibration of hadronically decaying tau leptons with the ATLAS experiment in pp collisions at* $\sqrt{s}$ = 8 *TeV*, Eur. Phys. J. C **75** (2015) 303, arXiv: 1412.7086 [hep-ex].

[96] ATLAS Collaboration, *Measurement of the tau lepton reconstruction and identification performance in the ATLAS experiment using pp collisions at* $\sqrt{s}$ = 13 *TeV*, ATLAS-CONF-2017-029, 2017, URL: https://cds.cern.ch/record/2261772.

[97] ATLAS Collaboration, *Reconstruction, Energy Calibration, and Identification of Hadronically Decaying Tau Leptons in the ATLAS Experiment for Run-2 of the LHC*, ATL-PHYS-PUB-2015-045, 2015, URL: https://cds.cern.ch/record/2064383.

[98] ATLAS Collaboration, *Measurement of the photon identification efficiencies with the ATLAS detector using LHC Run-1 data*, Eur. Phys. J. C **76** (2016) 666, arXiv: 1606.01813 [hep-ex].

[99] ATLAS Collaboration, *Performance of missing transverse momentum reconstruction with the ATLAS detector using proton–proton collisions at* $\sqrt{s}$ = 13 *TeV*, Eur. Phys. J. C **78** (2018) 903, arXiv: 1802.08168 [hep-ex].

[100] ATLAS Collaboration, *Performance of the missing transverse momentum triggers for the ATLAS detector during Run-2 data taking*, (2020), arXiv: 2005.09554 [hep-ex].

[101] ATLAS Collaboration, *Selection of jets produced in* 13 *TeV proton–proton collisions with the ATLAS detector*, ATLAS-CONF-2015-029, 2015, URL: https://cds.cern.ch/record/2037702.

[102] ATLAS Collaboration, *Characterisation and mitigation of beam-induced backgrounds observed in the ATLAS detector during the 2011 proton–proton run*, JINST **8** (2013) P07004, arXiv: 1303.0223 [hep-ex].

[103] ATLAS Collaboration, *Search for squarks and gluinos with the ATLAS detector in final states with jets and missing transverse momentum using* 4.7 fb^{-1} *of* $\sqrt{s}$ = 7 *TeV proton–proton collision data*, Phys. Rev. D **87** (2013) 012008, arXiv: 1208.0949 [hep-ex].

[104] G. Cowan, K. Cranmer, E. Gross and O. Vitells, *Asymptotic formulae for likelihood-based tests of new physics*, Eur. Phys. J. C **71** (2011) 1554, arXiv: 1007.1727 [physics.data-an], Erratum: Eur. Phys. J. C **73** (2013) 2501.

[105] ATLAS Collaboration, *Luminosity determination in pp collisions at* $\sqrt{s}$ = 8 *TeV using the ATLAS detector at the LHC*, Eur. Phys. J. C **76** (2016) 653, arXiv: 1608.03953 [hep-ex].

[106] ATLAS Collaboration, *The new LUCID-2 detector for luminosity measurement and monitoring in ATLAS*, JINST **13** (2018) P07017.

[107] ATLAS Collaboration, *Jet energy resolution in proton–proton collisions at* $\sqrt{s}$ = 7 *TeV recorded in 2010 with the ATLAS detector*, Eur. Phys. J. C **73** (2013) 2306, arXiv: 1210.6210 [hep-ex].

[108] ATLAS Collaboration, *Performance of pile-up mitigation techniques for jets in pp collisions at* $\sqrt{s}$ = 8 *TeV using the ATLAS detector*, Eur. Phys. J. C **76** (2016) 581, arXiv: 1510.03823 [hep-ex].

[109] ATLAS Collaboration, *Measurements of b-jet tagging efficiency with the ATLAS detector using* $t\bar{t}$ *events at* $\sqrt{s}$ = 13 *TeV*, JHEP **08** (2018) 089, arXiv: 1805.01845 [hep-ex].

[110] ATLAS Collaboration, *Electron reconstruction and identification in the ATLAS experiment using the 2015 and 2016 LHC proton–proton collision data at* $\sqrt{s}$ = 13 *TeV*, Eur. Phys. J. C **79** (2019) 639, arXiv: 1902.04655 [hep-ex].

[111] ATLAS Collaboration, *Electron and photon energy calibration with the ATLAS detector using 2015–2016 LHC proton–proton collision data*, JINST **14** (2019) P03017, arXiv: 1812.03848 [hep-ex].

[112] J. Butterworth et al., *PDF4LHC recommendations for LHC Run II*, J. Phys. G **43** (2016) 023001, arXiv: 1510.03865 [hep-ph].

[113] ATLAS Collaboration, *Studies on top-quark Monte Carlo modelling with Sherpa and MG5_aMC@NLO*, ATL-PHYS-PUB-2017-007, 2017, URL: https://cds.cern.ch/record/2261938.

[114] ATLAS Collaboration, *Studies on top-quark Monte Carlo modelling for Top2016*, ATL-PHYS-PUB-2016-020, 2016, URL: https://cds.cern.ch/record/2216168.

[115] L. A. Harland-Lang, A. D. Martin, P. Motylinski and R. S. Thorne, *Parton distributions in the LHC era: MMHT 2014 PDFs*, The European Physical Journal C **75** (2015) 204, ISSN: 1434-6052, URL: https://doi.org/10.1140/epjc/s10052-015-3397-6.

[116] A. L. Read, *Presentation of search results: the CL_S technique*, J. Phys. G **28** (2002) 2693.

[117] A. Boveia et al., *Recommendations on presenting LHC searches for missing transverse energy signals using simplified s-channel models of dark matter*, Physics of the Dark Universe **27** (2020) 100365, ISSN: 2212-6864, URL: http://www.sciencedirect.com/science/article/pii/S2212686419301633.

[118] M. Backović, A. Martini, O. Mattelaer, K. Kong and G. Mohlabeng, *Direct Detection of Dark Matter with MadDM v.2.0*, Phys. Dark Univ. **9-10** (2015) 37, arXiv: 1505.04190 [hep-ph].

[119] C. Amole et al., *Dark Matter Search Results from the Complete Exposure of the PICO-60 C_3F_8 Bubble Chamber*, Phys. Rev. D **100** (2019) 022001, arXiv: 1902.04031 [astro-ph.CO].

[120] D. Akerib et al., *Limits on spin-dependent WIMP-nucleon cross section obtained from the complete LUX exposure*, Phys. Rev. Lett. **118** (2017) 251302, arXiv: 1705.03380 [astro-ph.CO].

[121] E. Aprile et al., *Constraining the spin-dependent WIMP-nucleon cross sections with XENON1T*, Phys. Rev. Lett. **122** (2019) 141301, arXiv: 1902.03234 [astro-ph.CO].

[122] ATLAS Collaboration, *Search for scalar dark energy in $t\bar{t} + E_T^{miss}$ and mono-jet final states with the ATLAS detector*, ATL-PHYS-PUB-2018-008, 2018, URL: https://cds.cern.ch/record/2627837.